Journal of Nanobiotechnology

RESEARCH

Open Access

Cascade-targeting copper homeostasis nano-regulators for mild-photothermal boosted cuproptosis/ferroptosis mediated breast cancer therapy

Xuejun Liang[1,2†], Shiji Fang[3†], Yanan Xin[1,2], Jingju Lei[1,2], Wei Wang[2], Yi Wei[2], Wenhui Li[2], Chaojie Li[2], Hongchao Tang[4,5], Xian Wei[1], Yanqiang Huang[1], Lifei Zheng[1,2*], Yangping Shentu[6*], Xuli Meng[4,5*] and Xin Liu[7,2*]

Abstract

Inducing cuproptosis in tumor cells is significantly impeded by the challenges of arduous copper ion delivery *in vivo* and the unbreakable intracellular copper homeostasis, which leads to insufficient mitochondrial copper accumulation. Here, a carrier-free metal-polyphenolic (CF-MPs) based nanoplatform (T-T@Cu) that features tumor-mitochondria cascade-targeting, glutathione (GSH) depletion and near-infrared Ⅱ photothermal performance is designed to induce mitochondria copper-overload and exacerbate cuproptosis in tumor cells. By leveraging the enhanced permeability and retention (EPR) effects and the mitochondria-targeting capabilities of tannic acid, T-T@Cu effectively increases mitochondrial copper accumulation in tumor cells. Upon exposure to a 1064 nm laser, T-T@Cu triggers mild photothermal-boosted ferroptosis, which down-regulates intracellular ATP levels. This reduction dramatically impacts the expression of copper-ion efflux proteins ATP7A/7B, ultimately inhibiting copper ion efflux. Additionally, T-T@Cu exhibits robust GSH consumption and dual-responsive degradation in tumor microenvironments characterized by overexpressed cysteine (Cys) and GSH. This results in alleviated GSH-induced inactivation of copper ions and specific copper release within the tumor microenvironment. In vitro and *in vivo* therapeutic evaluations demonstrate the outstanding tumor inhibition of T-T@Cu in 4T1-breast-cancer models, with no significant systemic toxicity observed. This novel mild photothermal-boosted ferroptosis strategy for exacerbating tumor cell cuproptosis holds great promise for future clinical applications in oncotherapy.

Keywords Mild-photothermal, Cuproptosis, Ferroptosis, Copper homeostasis, GSH depletion

†Xuejun Liang and Shiji Fang contributed equally to this work.

*Correspondence:
Lifei Zheng
zhenglf@ucas.ac.cn
Yangping Shentu
styp@wmu.edu.cn
Xuli Meng
mxlmail@126.com
Xin Liu
lx@ucas.ac.cn

Full list of author information is available at the end of the article

Graphical abstract

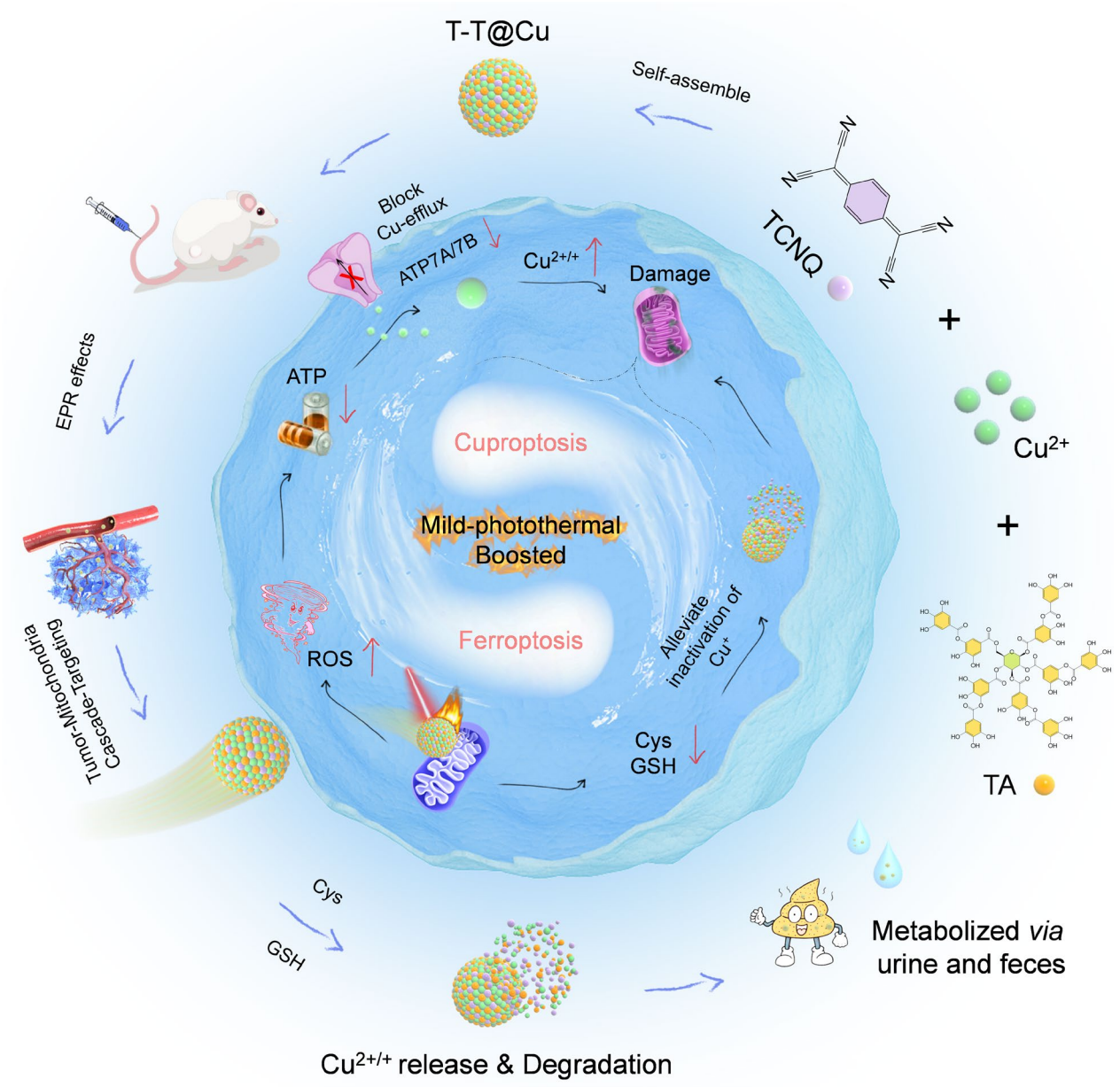

Introduction

Cuproptosis was recently identified by Tsvetkov et al. as a novel programmed cell death (PCD) modality characterized by copper-induced lipoylated protein aggregation and the loss of iron-sulfur (Fe-S) cluster proteins in the mitochondrial tricarboxylic acid (TCA) cycle [1]. This process arises from mitochondrial copper overload and culminates in cell death due to proteotoxic stress. Despite being in its infancy, cuproptosis has aroused significant interest in oncotherapy, as multiple refractory malignancies, including drug-resistant tumors, are susceptible to this form of cell death [2–4]. However, before cuproptosis can be widely applied in clinical settings, several challenges must be addressed [5]. Notably, the poor targeting of copper ions to tumor mitochondria and the difficulty in overcoming intracellular copper homeostasis present significant obstacles to achieving mitochondrial copper overload, which is crucial for inducing cuproptosis in tumor cells [6–9]. Additionally, the low selectivity of cuproptosis between normal and tumor cells raises potential biosafety concerns [10, 11]. Therefore, it is imperative to explore strategies for efficiently inducing

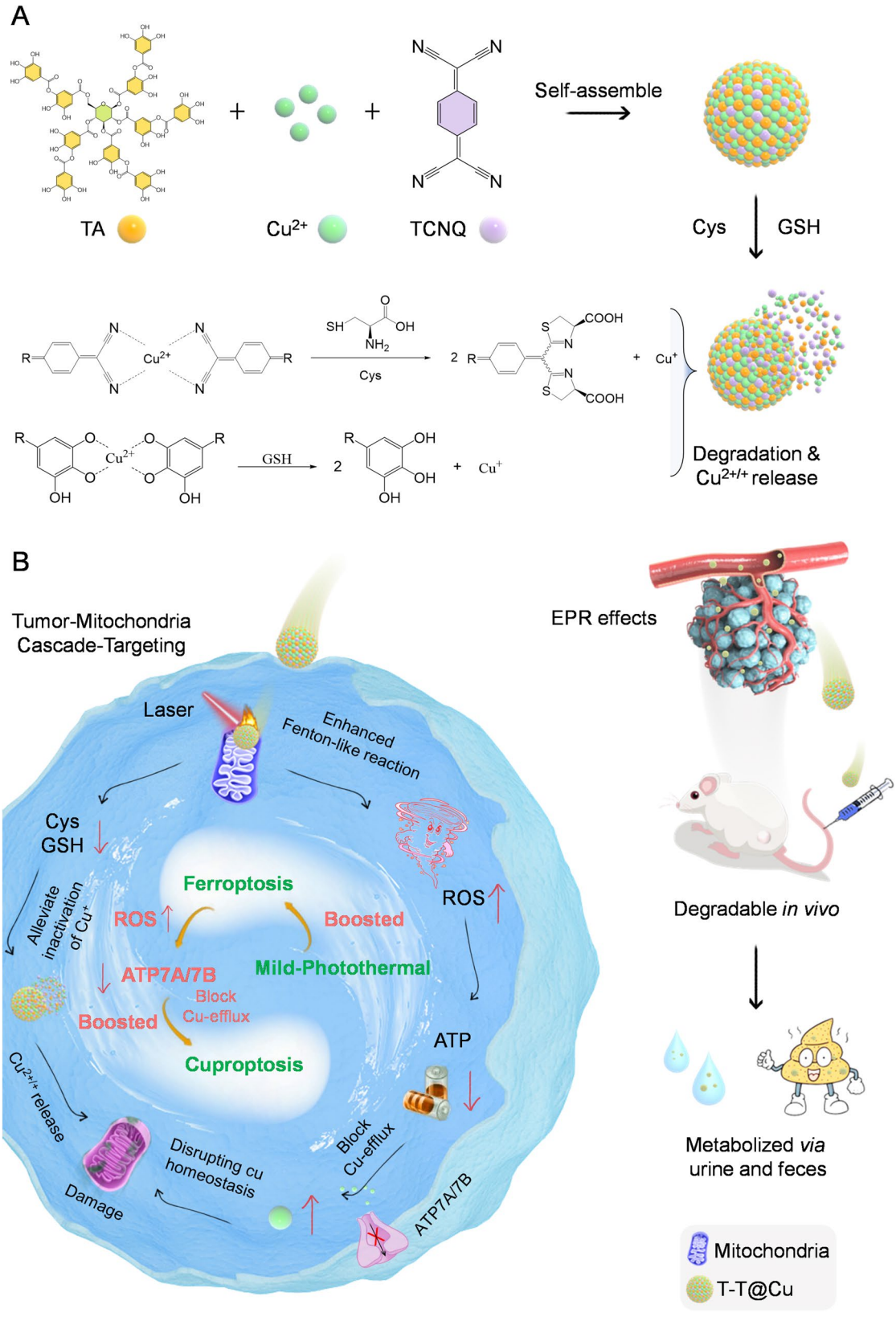

Fig. 1 (See legend on next page.)

(See figure on previous page.)

Scheme 1 Preparation of T-T@Cu for exacerbating tumor cell cuproptosis. (**A**) Schematic illustration showing the preparation and Cys/GSH-responsive degradation mechanism of T-T@Cu. (**B**) The biological mechanism of exacerbated tumor cell cuproptosis induced by T-T@Cu. T-T@Cu can effectively accumulates at tumor sites of CDA^{4T1} mouse models *via* intravenous injection and specifically targets the mitochondria of tumor cells. Once irradiated by a 1064 nm NIR II laser, T-T@Cu can down-regulate intracellular ATP levels *via* mild-photothermal boosted ferroptosis, leading to disruption of the activity and expression of copper-ion efflux proteins (ATP7A/7B). Meanwhile, T-T@Cu can prevent the GSH-induced inactivation of copper ions *via* depleting overexpressed Cys and GSH in tumor cells. These processes significantly enhanced mitochondrial copper overload, which facilitates the proteotoxic aggregation of DLAT and destabilized Fe-S cluster proteins, hence exacerbating tumor cells cuproptosis

cuproptosis in tumor cells while minimizing damage to normal cells.

Due to the short blood circulation half-life and non-specific targeting of copper ions, the induction of cuproptosis in tumor cells heavily relies on copper ion delivery systems that can selectively transport copper ions into the mitochondria of tumor cells. While numerous copper ion delivery systems, including copper ionophores, inorganic nanoparticles (NPs), and biomacromolecules, have been successfully developed, most focus primarily on enhancing the tumor enrichment of copper ions [12–16]. The mitochondrial targeting efficiency of these copper ions, which is crucial for effectively inducing cuproptosis in tumor cells, is often overlooked. Although some nanosystems based on elesclomol and triphenylphosphine have been designed to achieve tumor-mitochondria cascade targeted delivery of copper ions, their clinical applications are hindered by high costs and unknown long-term biosafety due to complex preparation processes and non-degradability *in vivo* [17, 18]. Carrier-free metal-polyphenolic nanocomplexes (CF-MPs), formed by the self-assembly of metal ions and polyphenols through coordination interactions, have garnered significant attention in the field of oncotherapy due to their easy preparation, tumor-specific targeting, and high metal ion loading capacity [19–21]. Tannic acid (TA), a plant-derived natural polyphenol, is particularly notable as a building block for CF-MPs, owing to its excellent biological properties, including biodegradability and strong protein affinity [22–25]. Given TA's robust non-covalent affinity for mitochondrial outer membrane proteins, we speculate that it may serve as an ideal candidate for developing tumor-mitochondria cascade targeted copper ion delivery systems.

Furthermore, to prevent intracellular copper overload, tumor cells have evolved a sophisticated copper homeostasis regulation system [26]. When excess copper ions are internalized by tumor cells, they face the risk of being either expelled by copper-ion efflux proteins ATP7A and ATP7B (ATP7A/7B) or inactivated by overexpressed intracellular glutathione (GSH) [27–30]. This process can lead to insufficient mitochondrial copper accumulation, which is necessary to trigger effective cuproptosis in tumor cells. Therefore, in addition to exploring ideal tumor-mitochondria cascade targeted copper ion delivery systems, breaking intracellular copper homeostasis is another critical factor for enhancing cuproptosis in tumor cells. Ferroptosis, a non-apoptotic programmed cell death modality characterized by oxidative damage to plasma membranes and mitochondria, has been demonstrated to disrupt cellular energy metabolism through mitochondrial adenosine triphosphate (ATP) depletion [31]. Given that copper-transporting ATPases (ATP7A/7B) depend on ATP hydrolysis to facilitate copper ion efflux [32], the ferroptosis-associated decline in ATP levels may compromise their function, resulting in intracellular copper accumulation. Furthermore, ferroptosis generates excessive reactive oxygen species (ROS) and lipid peroxides (LPO), which can directly oxidize and impair ATP7A/7B transporters, exacerbating copper homeostasis dysregulation [33]. Based on these findings, we propose that ferroptosis induction in tumor cells may suppress ATP7A/7B-mediated copper efflux, thereby disrupting intracellular copper homeostasis. However, the poor Fenton reaction activity between Fe^{2+} and H_2O_2 in acidic tumor microenvironments (TME) results in insufficient ROS generation for effective ferroptosis induction [34]. Given that copper ions exhibit higher Fenton-like catalytic activity than Fe^{2+} in the TME, which can be further enhanced by mild-photothermal effects, we propose that mild photothermal-boosted ferroptosis triggered by copper ion-based nanosystems could effectively down-regulate the expression of ATP7A/7B [35]. This down-regulation may alleviate copper ion efflux and exacerbate cuproptosis in tumor cells.

Herein, we developed a versatile carrier-free metal-polyphenolic nanocomplex-based nanoplatform (T-T@Cu) to induce robust cuproptosis in tumor cells through efficient tumor-mitochondria cascade-targeted delivery of copper ions and regulation of intracellular copper homeostasis. As illustrated in Scheme 1, T-T@Cu was constructed by the simple self-assembly of tannic acid (TA), 7,7,8,8-tetracyanoquinodimethane (TCNQ), and copper ions *via* coordination and charge transfer (CT) interactions. As a natural polyphenol, TA not only specifically binds to mitochondrial outer membrane proteins but also forms CT nanocomplexes with excellent near-infrared (NIR) II (1000–1700 nm) photothermal performance in conjunction with copper ions and TCNQ. To prevent the inactivation of copper ions by overexpressed glutathione (GSH) in tumor cells, TCNQ is employed to consume cysteine (Cys), an essential amino acid for GSH biosynthesis. Following intravenous injection of T-T@Cu in 4T1 cell line-derived allograft (CDA^{4T1}) mouse

models, T-T@Cu effectively accumulates at tumor sites *via* enhanced permeability and retention (EPR) effects and specifically targets the mitochondria of tumor cells. Upon exposure to a 1064 nm NIR II laser, T-T@Cu triggers mild-photothermal boosted ferroptosis, impacting the activity and expression of copper-ion efflux proteins (ATP7A/7B). This process leads to enhanced mitochondrial copper overload and exacerbates cuproptosis in tumor cells. Notably, due to the low sensitivity of normal cells to ferroptosis, this novel cuproptosis strategy mediated by T-T@Cu demonstrates extraordinary tumor cell-specific killing effects without damaging normal cells, highlighting its promising potential in oncotherapy.

Experimental section

Preparation of T-T@Cu

10 mg of TCNQ, 26 mg of $CuCl_2$ and 82 mg of TA were co-dissolved in N, N-dimethylformamide (DMF). 15 mL of pure water was added dropwise to the above mixed solution under ultrasonic treatment at room temperature. After continued 5 min of ultrasonic treatment, the as-prepared T-T@Cu was washed with pure water for several time *via* centrifugation (13000 rpm, 10 min) and re-dispersed in PBS 7.4 for usage.

In vitro biodegradability test of T-T@Cu

T-T@Cu was dispersed in PBS (pH 4.0) and PBS (pH 7.4) with different concentrations of Cys (15 μM, 200 μM and 400 μM), GSH (20 μM, 1 mM and 10 mM) or Cys + GSH (15 μM + 20 μM, 200 μM + 1 mM and 400 μM + 10 mM), respectively. At predesigned time intervals, the digital photos, absorbance at 808 nm and size distribution of T-T@Cu were recorded to investigate the biodegradation process.

In vitro Cys and GSH consumption assay

0.5 mL of Cys or GSH PBS 7.4 solution was mixed with 0.5 mL of T-T@Cu dispersion with various concentrations. After incubation for 3 h, the mixed solution was subsequently centrifuged (13000 rpm, 10 min). The supernatant was collected for determining the Cys or GSH level *via* measure the residual -SH groups of Cys and GSH using 5,5'-Dithiobis-(2-nitrobenzoic acid) (DTNB) as a -SH indicator.

In vitro Cu release assay

0.5 mL of T-T@Cu dispersion sealed in dialysis bag (MWCO ≈ 1000 Da) was soaked in PBS (pH 7.4) with different concentrations of Cys (15 μM, 200 μM, 400 μM), GSH (20 μM, 1 mM, 10 mM) or Cys + GSH (15 μM + 20 μM, 200 μM + 1 mM and 400 μM + 10 mM), followed by incubating at 37 ℃. At predesigned time intervals, 1 mL of dialysate was collected before replenishing with 1 mL corresponding fresh PBS. The Cu content in collected dialysate was detected *via* ICP-MS and the cumulative release curve of Cu was plotted.

In vitro detection of hydroxyl radical (•OH)

2 mL of T-T@Cu dispersion containing H_2O_2 and TMB were incubated at room temperature. During this process, T-T@Cu + H_2O_2 + TMB + L treatment group received an extra irradiation by a 1064 nm laser (1W/cm^2). H_2O_2 + TMB and H_2O_2 + TMB + L treatment groups were served as controlled groups. At different time intervals, the absorption at the range of 500 nm to 900 nm was recorded for evaluation of the •OH generation.

1 mL of T-T@Cu dispersion containing H_2O_2 was incubated at room temperature or oil bath (45℃) for 12 min. The ESR signals of different treatment groups were recorded by an ESR spectrometer (EMXplus-6/1, Bruker) at pre-designed time intervals. 5,5-dimethyl-1-pyrroline N-oxide (DMPO) was employed to trap •OH indicator. H_2O_2, H_2O_2 + 45℃ and T-T@Cu treatment groups were set as control groups.

Cell culture and cytotoxicity study

Human umbilical vein endothelial cells (HUVEC), Human hepatocellular carcinomas (HepG2) and Mouse breast cancer cells (4T1) were purchased from the cell bank of the Chinese Academy of Sciences (Shanghai, China). All the cells were cultured in the corresponding cell culture medium supplemented with 10% (v/v) fetal bovine serum at 37 ℃ under a 5% CO_2 humid atmosphere.

HUVEC, HepG2 and 4T1 cells were seeded in 96-well plates and cultured overnight before cytotoxicity assay. The cells were then incubated with $CuCl_2$ and T-T@Cu of various copper concentrations for another different hours (8 h and 24 h). In addition, cells in laser treatment group (T-T@Cu + laser and T-T@Cu + ammonium tetrathiomolybdate (ttm) + laser) were irradiated by a 1064 nm laser (1 W/cm^2). PBS, $CuCl_2$ and T-T@Cu plus ttm treated cells were regarded as control groups. The cell viability was evaluated by a standard Cell Counting Kit-8 (CCK-8) Assay.

Mitochondrial targeting validation

4T1 cells were incubated in 1640 medium with RhB@T-T@Cu for 6 h. Before confocal laser scanning microscopy (CLSM) observation, the cells were stained by DAPI and Mito-tracker Green.

The mitochondria from 4T1 cells treated with PBS, $CuCl_2$ and T-T@Cu for 8 h were isolated by the Cell Mitochondria Isolation Kit. Firstly, the 4T1 cells in various treatment groups were collected and well homogenized. Subsequently, mitochondria were separated from the cell homogenates *via* two steps of centrifugation at 4

℃. The isolated mitochondria were digested and used for copper quantification by ICP-MS.

Determination of intracellular GSH and Cys

4T1 cells were seeded in 6-well plates and cultured overnight. The cells were incubated with $CuCl_2$ and T-T@Cu at various mass concentrations for 8 h. After thoroughly washed with ice-cold PBS, the intracellular GSH and Cys levels were measured by a Reduced GSH Content Assay Kit and a Cys Colorimetric Assay Kit, respectively.

Validation of DLAT aggregation

4T1 cells were seeded onto a glass coverslip in 24-well plate and cultured overnight. The cells were divided into seven groups (PBS, PBS + L, $CuCl_2$, T-T@Cu, T-T@Cu + ttm, T-T@Cu + ttm + L, T-T@Cu + L) and incubated with various drugs at fixed Cu (3 μg/mL) and ttm (5 μg/mL) concentrations for 8 h. The cells in the irradiation groups received an extra 1064 nm laser (1 W/cm^2) irradiation. Afterward, the cells were washed thoroughly with ice-cold PBS and fixed with 4% paraformaldehyde at 4℃. Before CLSM observation, the cells were incubated sequentially with corresponding primary and secondary antibodies. The cell nuclei were stained by DAPI.

Evaluation of intracellular ROS and LPO

4T1 cells were seeded in 24-well plates and cultured till monolayer growth. Subsequently, the cells were further cultured with T-T@Cu (25 μg/mL) for 9 h. During this process, the cells in T-T@Cu + L treatment group received an extra irradiation by a 1064 nm laser (1 W/cm^2). PBS treated cells were served as blank control group. Before the flow cytometry analysis, the cells in different treatment groups were collected, washed by ice-cold PBS and stained by DCFH-DA or BODIPY™ 581/591 C11.

RNA-sequencing analysis

4T1 cells were seeded in 6-well plate at a density of 1×10^6 per well. After 24 h of incubation, the cells received various treatments including PBS, PBS + L, $CuCl_2$, T-T@Cu and T-T@Cu + L. The cells in the irradiation groups were irradiated by a 1064 nm laser (1 W/cm^2). TRIzol reagent (Invitrogen, CA, USA) was used to extract total RNA. VAHTS Universal V6 RNA-seq Library Prep Kit was used to construct the libraries. Illumina Novaseq 6000 was applied in RNA sequencing. Fastp[1] was used to quantify the transcription levels. R (v 3.2.0) was employed to generate the volcano graphs and the heat maps. R (v 3.2.0) also utilized to complete the Kyoto Encyclopedia of Genes and Genomes (KEGG) pathway and Gene Ontology (GO) pathway enrichment analysis. GSEA software was used to perform the Gene Set Enrichment Analysis (GSEA). Cytoscape was utilized to generate the protein-protein interaction (PPI) network.

Photothermal induced in vivo infrared thermal imaging

4T1 allograft tumor-bearing mice were administered intravenously with PBS and PBS suspension of T-T@Cu (4.4 μg NPs/g body weight). After 3 h of administration, the tumors of the mice were irradiated by a 1064 nm laser (1 W/cm^2, 80 s). Meanwhile, the *in vivo* infrared thermal images and temperature variation of tumors were recorded by an infrared thermal camera (FLIR A300).

In vivo bio-distribution study

36 of 4T1 allograft tumor-bearing mice were randomly divided into two groups and received intravenous injection of PBS and PBS suspension of RhB@T-T@Cu (5 μg NPs/g body weight). Thereafter, at pre-designed time intervals (1 h, 3 h, 6 h, 10 h, 13 h and 24 h), three mice were randomly picked up from each group and sacrificed for harvesting their main organs. The ex vivo fluorescence imaging of the dissected organs was acquired an IVIS Lumina XRMS Series III small animal imaging system. The PBS treated mice were served as blank control group.

In vivo metabolism of T-T@Cu

4T1 allograft tumor-bearing mice were randomly grouped and injected intravenously with PBS and PBS suspension of T-T@Cu (5 μg NPs/g body weight). At pre-designed time intervals (6 h, 12 h, 36 h, 48 h and 72 h), the urine and feces of mice were collected by using metabolic cages. The copper content in the urine and feces was quantified by ICP-MS.

Evaluation of in vivo therapeutic efficacy

When the tumor volume reached about 100 mm^3, 35 of 4T1 allograft tumor-bearing mice were randomly grouped and treated with PBS, PBS + L, $CuCl_2$, T-T@Cu, T-T@Cu + ttm, T-T@Cu + ttm + L and T-T@Cu + L, respectively. The administrated drug concentration of copper and ttm in various treatment groups were fix at 0.8 μg/g body weight and 5 μg/g body weight, respectively. During the treatment duration, the mice in each group received three doses of different drugs, and the tumors of the mice were irradiated by a 1064 nm laser (1 W/cm^2) every three day within the first 9 days of treatment. The tumor volume and body weight variations of mice were recorded every day for evaluating the therapeutic efficacy. On the 3th day of treatment, one mouse was randomly selected from each group and its tumor was dissected for FDX1, LIAS, DLAT, GPX4, TUNEL and H&E staining observation.

Results and discussion

Preparation and characterization of T-T@Cu

Equimolar amounts of TA and TCNQ, serving as donor (D) and acceptor (A) molecules, respectively, have been shown to form greenish CT complexes with near-infrared (NIR) absorption in dimethyl formamide (DMF) (Fig. 1A&S1). Additionally, TA, as a natural polyphenolic compound, can form metal-polyphenol complexes with copper ions (Cu^{2+}) through oxidative-mediated self-assembly. This interaction is evidenced by the bathochromic shift of the absorption peak of TA from 275 nm to 310 nm in the UV-Vis-NIR absorption spectrum of the TA@Cu complexes (Fig. S2). Given these intermolecular interactions, we hypothesize that the combination of TA, TCNQ, and Cu^{2+} can form CT nanocomplexes with potential NIR absorption properties.

Herein, a carrier-free metal-polyphenol nanoplatform (T-T@Cu) was prepared *via* a nanoprecipitation method

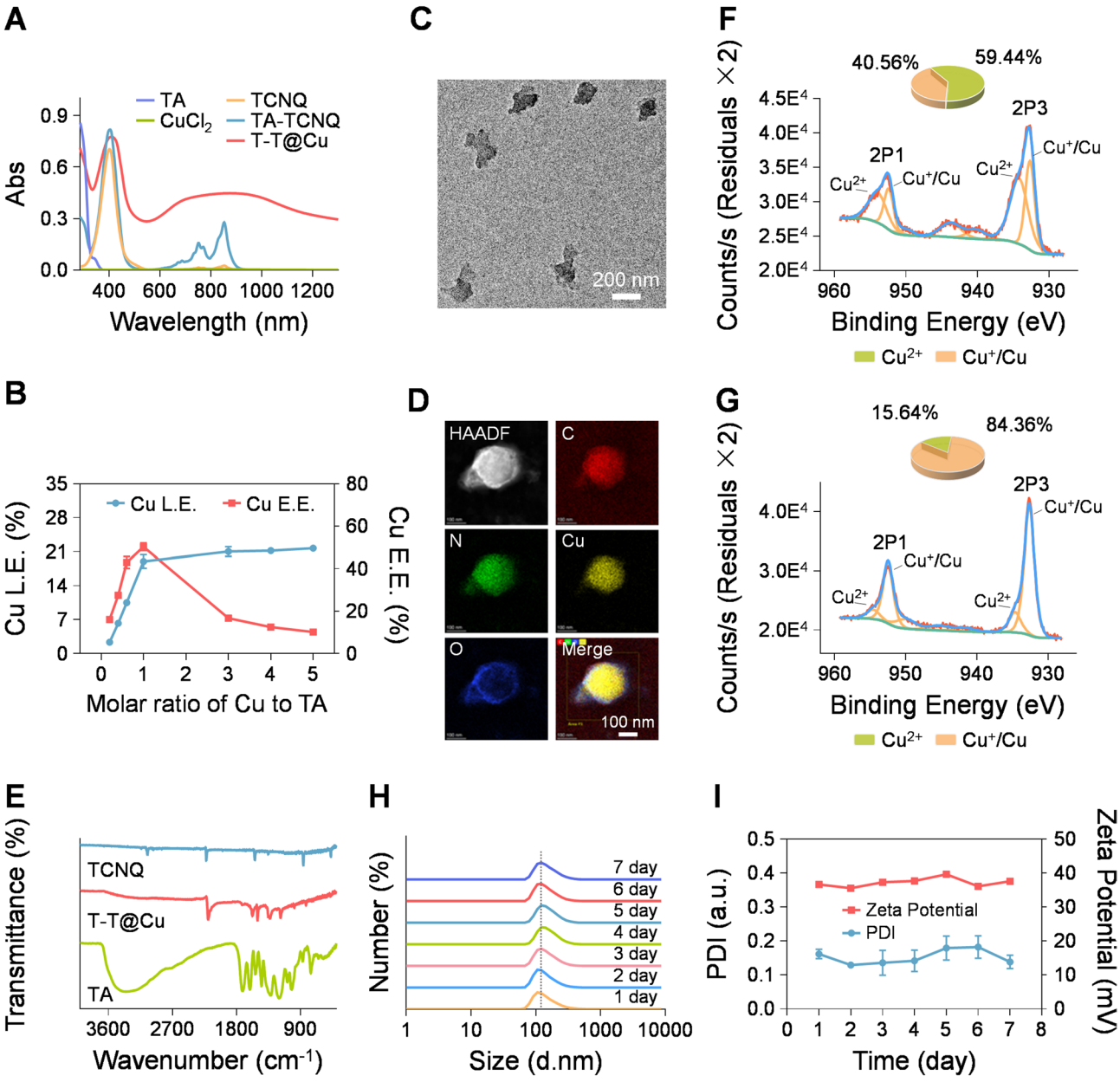

Fig. 1 Structural and performance characterization of T-T@Cu. **A**) Ultraviolet-visible-near-infrared (UV-vis-NIR) absorption spectra of TA, $CuCl_2$, TCNQ, TA-TCNQ and T-T@Cu. **B**) Copper loading efficiency (L.E.) and encapsulation efficiency (E.E.) of T-T@Cu. **C**) Representative TEM image of T-T@Cu. The bar value is 200 nm. **D**) High-angle annular dark-field (HAADF) TEM image and elemental mapping images of C, N, O and Cu atoms in T-T@Cu. The bar value is 100 nm. **E**) FTIR spectra of TA, TCNQ and T-T@Cu. High-resolution XPS spectra of copper in T-T@Cu **F**) before and **G**) after GSH reduction. **H**) DLS analysis of the hydrodynamic sizes of T-T@Cu in PBS (pH 7.4) during 7 days. **I**) PDI and Zeta potential variation of T-T@Cu in PBS (pH 7.4) during 7 days

by adding pure water to the mixed DMF solution of $CuCl_2$, TA and TCNQ under ultrasonic conditions. To optimize the feeding ratio of TA, TCNQ, and Cu^{2+} for the preparation of T-T@Cu, we systematically studied the morphology, size distribution, and UV-Vis-NIR absorption spectra of the as-prepared T-T@Cu. Transmission electron microscopy (TEM) images revealed that the as-prepared T-T@Cu exhibited various morphologies and sizes. By fixing the molar ratio of TA and TCNQ at 1:1, we observed that the size of T-T@Cu increased with the feeding ratio of Cu^{2+} (Fig. S3&S4). This increase in size can be attributed to the higher feeding ratio of Cu^{2+}, which provides sufficient copper ions to crosslink the TA-TCNQ CT complexes, resulting in larger T-T@Cu particles. Meanwhile, the copper loading efficiency (L.E.) and encapsulation efficiency (E.E.) were measured, with maximum values determined to be approximately 22% and 51%, respectively, at feeding ratios of TA, TCNQ, and Cu^{2+} of 1:1:5 and 1:1:0.8 (Fig. 1B). Additionally, the absorption peak of T-T@Cu exhibited a bathochromic shift into the NIR II bio-window (1000–1700 nm) and increased slightly with the feeding ratio of Cu^{2+} (Fig. 1A&S5). We speculate that the presence of Cu^{2+} facilitates the delocalization of p-electrons from the highest occupied molecular orbital of TA (D) to the lowest unoccupied molecular orbital of TCNQ (A), leading to a significant reduction in the energy gap and a corresponding redshift in absorption [36, 37]. When the feeding ratio of TA, TCNQ, and Cu^{2+} was 1:1:4, we obtained cauliflower-shaped T-T@Cu with concentration-dependent NIR II absorption (Fig. S6) and a suitable size (~ 120 nm) for *in vivo* administration (Fig. 1C). Elemental mapping images confirmed the uniform distribution of C, O, N and Cu, validating the successful preparation of T-T@Cu (Fig. 1D). Fourier transform infrared (FTIR) spectroscopy further verified the composition of T-T@Cu, showing characteristic peaks at 2200 cm^{-1} and 1600 cm^{-1} corresponding to TCNQ, and peaks at 1300 cm^{-1} and 1200 cm^{-1} associated with TA. Notably, the disappearance of the hydroxyl stretching vibration peak at 3400 cm^{-1} in T-T@Cu indicates the oxidation of TA by coordinated copper ions. Moreover, the intensity decay of peaks at 1315 cm^{-1} and 1189 cm^{-1} suggests distortion of TA due to coordination with copper ions (Fig. 1E). High-resolution X-ray photoelectron spectroscopy (HR-XPS) was conducted to investigate the oxidation state of copper in T-T@Cu. Both Cu^{2+} and Cu^{+} binding energy peaks, along with strong satellite peaks, were detected, indicating that approximately 40.56% of Cu^{2+} was reduced to Cu^{+} by the phenolic hydroxyl groups of TA (Fig. 1F). Importantly, we found that Cu^{2+} in T-T@Cu can be further reduced to Cu^{+} by GSH (Fig. 1G), suggesting that T-T@Cu may release Cu^{+} in response to the tumor microenvironment, which is characterized by overexpressed GSH, thereby facilitating cuproptosis in tumor cells. Dynamic light scattering (DLS) analysis showed that the hydrodynamic diameter of as-prepared T-T@Cu in PBS (pH 7.4) was approximately 122 nm and remained nearly constant over seven days (Fig. 1H). The polydispersity index (PDI) and zeta potential were maintained around ~ 0.15 and – 37 mV, respectively, throughout the week, indicating excellent stability of T-T@Cu in PBS (pH 7.4) (Fig. 1I).

Cys and GSH dual-response degradation of T-T@Cu

The tumor microenvironment (TME) is characterized by distinct metabolic features that create unique conditions for drug delivery and efficacy. The development of nanodrugs with TME-responsive degradability is crucial for achieving high tumor-specific killing efficacy while minimizing systemic toxicity [38]. T-T@Cu leverages the specific interactions between Cys and aryl nitriles, as well as the redox reactions involving transition metal ions (i.e. Cu^{2+}) and the thiol (-SH) groups in GSH [39, 40]. Therefore, the overexpressed Cys and GSH in tumor tissues as endogenous stimulus can trigger the degradation of T-T@Cu. As illustrated in Fig. 2A, when TCNQ was mixed with Cys in dimethyl sulfoxide (DMSO), a bathochromic shift of the absorption peak from 405 nm to 420 nm was observed. This shift confirmed the formation of mono-thiazolidine derivatives resulting from the reaction between TCNQ and Cys. Additionally, a new absorption peak around 485 nm emerged, likely due to the formation of bi-substituted and multi-substituted compounds (Fig. S7). The redox reaction between Cu^{2+} ions and the -SH groups of GSH was investigated using 5,5'-Dithiobis-(2-nitrobenzoic acid) (DTNB) as a -SH indicator. As shown in Fig. 2B, the intensity of the absorption peak at 412 nm, which corresponds to the reaction products of -SH and DTNB, progressively decreased with increasing concentrations of Cu^{2+}. This result indicated that Cu^{2+} ions effectively consume the -SH groups of GSH through a redox reaction. Furthermore, in vitro studies were conducted to measure the residual -SH groups of both Cys and GSH after treatment with T-T@Cu. The results demonstrated that T-T@Cu can react with Cys and GSH simultaneously, and the consumption of Cys and GSH by T-T@Cu occurred in a dose-dependent manner (Fig. 2C).

To evaluate the stability of T-T@Cu *in vivo*, photographs of T-T@Cu in various media, including mimic plasma (PBS (pH 7.4) with Cys (15 μM), GSH (20 μM) or Cys (15 μM) + GSH (20 μM)), mimic intracellular lysosomal microenvironment (PBS (pH 4.0)), mimic intracellular microenvironments of normal cells (PBS (pH 7.4) with Cys (200 μM), GSH (1 mM) or Cys (200 μM) + GSH (1 mM)) and tumor cells (PBS (pH 7.4) with Cys (400 μM), GSH (10 mM) or Cys (400 μM) + GSH (10 mM)), were recorded at predesigned time intervals (Fig. S8). Negligible color change was observed in the mimic

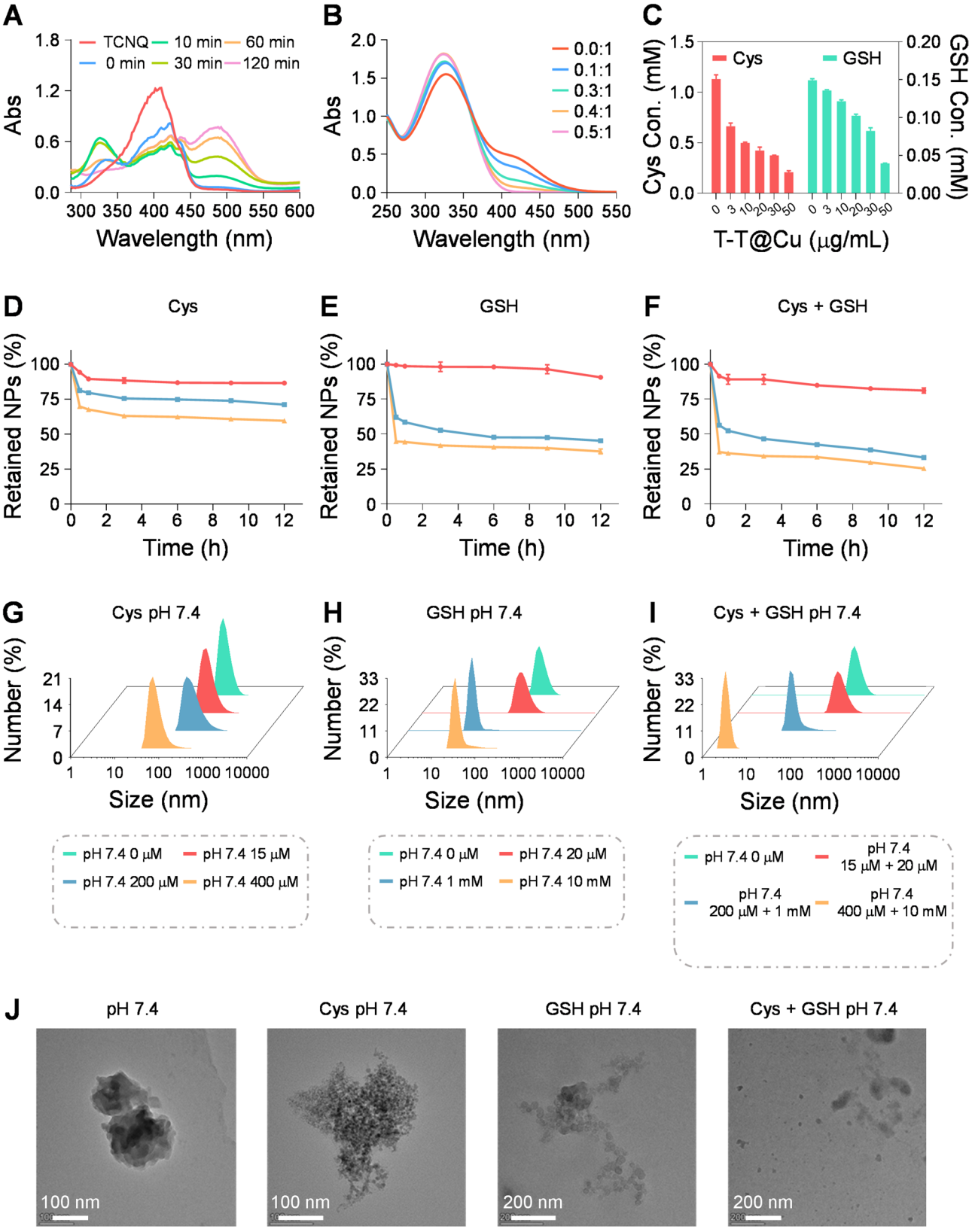

Fig. 2 (See legend on next page.)

(See figure on previous page.)

Fig. 2 In vitro evaluation of Cys and GSH dual-responsive degradation of T-T@Cu. **A**) UV-vis absorption spectra of TCNQ obtained at different reaction time with Cys. **B**) UV-vis absorption spectra of DTNB in GSH solution with Cu^{2+} at different concentrations. **C**) Concentration dependent Cys and GSH consumption by T-T@Cu. **D-F**) Degradation kinetics of T-T@Cu in various mimic *in vivo* microenvironments including plasma, intracellular microenvironments of normal cells and tumor cells. **G-I**) DLS analysis of the hydrodynamic size variations of T-T@Cu in various mimic *in vivo* microenvironments. **J**) TEM images of T-T@Cu in various mimic *in vivo* microenvironments for 6 h

plasma and intracellular lysosomal microenvironment dispersion of T-T@Cu within 12 h, suggesting satisfactory stability during the blood circulation and lysosomal internalization process. In contrast, T-T@Cu gradually faded in the mimic intracellular microenvironments of both normal and tumor cells, with a faster fading rate noted in the latter. The results indicated that T-T@Cu might undergo degradation after being internalized by both normal and tumor cells. Subsequently, the degradation ratios of T-T@Cu in various media were analyzed by recording its absorption variation at 808 nm. As shown in Fig. 2D and F, T-T@Cu exhibited the highest degradation ratios of approximately 40%, 62%, and 75% in the mimic intracellular microenvironment of tumor cells (PBS (pH 7.4) with Cys (400 mM), GSH (10 mM), or Cys (400 mM) + GSH (10 mM)) within 12 h [41, 42]. This indicated that T-T@Cu could degrade more thoroughly in tumor cells, especially in the intracellular microenvironment containing both Cys and GSH. In comparison, T-T@Cu exhibited lower degradation ratios in mimic plasma, intracellular lysosomal microenvironment and the intracellular microenvironments of normal cells. Notably, the degradation ratio of T-T@Cu in mimic plasma and intracellular lysosomal microenvironment within 12 h was determined to be ~ 19% and 9.3%, validating that T-T@Cu can remain relatively intact during the blood circulation and lysosomal internalization process (Fig. 2F&S9). DLS and TEM analysis further demonstrated that T-T@Cu can undergo degradation in the mimic intracellular microenvironments of tumor cells, dissociating into ultra-small nanoparticles (NPs) with diameters of less than 5 nm (Fig. 2G and J). Since NPs smaller than 5 nm are reported to be capable of urinary metabolism, we speculate that the degradation products of T-T@Cu can eventually be metabolized.

In vitro copper ion release and •OH generation

Then, the release of copper ions from T-T@Cu in various media was systematically studied using inductively coupled plasma mass spectrometry (ICP-MS). The final released copper ions in the mimic intracellular microenvironments of tumor cells reached ~ 93% within 96 h, which was significantly higher than the release observed in mimic plasma (~ 38%) and the intracellular microenvironment of normal cells (~ 73%) (Fig. 3A). This specific copper ion-responsive release in tumor microenvironments may be beneficial for triggering ferroptosis and cuproptosis in tumor cells. To validate the Fenton-like reaction between T-T@Cu and H_2O_2, the catalytic activity of T-T@Cu for •OH generation was investigated. The oxidation of 3,3',5,5'-tetramethylbenzidine (TMB) by •OH results in a measurable change in absorption intensity at 652 nm, which indicates •OH generation. In T-T@Cu + H_2O_2 + TMB and T-T@Cu + H_2O_2 + TMB + L treatment groups, the absorption intensity of TMB at 652 nm progressively increased over time (Fig. S10A&3B), while negligible changes were detected in the absorption curves of TMB + H_2O_2 and TMB + H_2O_2 + L treatment groups (Fig. S10B&S10C). Additionally, the electron spin resonance (ESR) spectra of different treatment groups were measured using 5,5-dimethyl-1-pyrroline N-oxide (DMPO) as a trapping agent for •OH. The characteristic quartets (1:2:2:1) of the DMPO/•OH adduct were observed in $CuCl_2$ + H_2O_2, T-T@Cu + H_2O_2 and T-T@Cu + H_2O_2 + 45℃ treatment groups, but not in T-T@Cu, $CuCl_2$ and H_2O_2 treatment groups. Notably, the characteristic signals of •OH were significantly enhanced with a mild-photothermal (45℃) treatment (Fig. 3C). The above results verified the Fenton-like catalytic activity of T-T@Cu for •OH generation, which could be dramatically enhanced by mild-photothermal effects.

Photothermal performance

Based on the outstanding absorption in NIR II bio-window, the NIR II photothermal performance of T-T@Cu was systematically studied. When exposed to a 1064 nm NIR II laser, the photothermal performance of T-T@Cu was found to be dependent on both concentration and laser power density. After 6 min of irradiation with a 1064 nm laser (1 W/cm^2), the temperature of T-T@Cu aqueous solutions at various concentrations (20 μg/mL, 30 μg/mL, 40 μg/mL, 80 μg/mL and 200 μg/mL) rose from 28℃ to 44℃, 48℃, 52℃, 61℃ and 71℃, respectively (Fig. 3D). Moreover, for 80 μg/mL T-T@Cu aqueous solution, the ultimate temperatures after 6 min of irradiation with different power densities (0.5 W/cm^2, 1 W/cm^2 and 1.5 W/cm^2) were measured to be 43℃, 61℃ and 68℃, respectively (Fig. 3E). Corresponding infrared thermal imaging photos of T-T@Cu aqueous solutions subjected to different doses of irradiation further demonstrated its excellent photothermal performance (Fig. 3F). The photothermal conversion efficiency (h) of T-T@Cu at 1064 nm was calculated using a standard detection method. As shown in Fig. 3G and H, the h value of T-T@Cu was measured to be ~ 48.5%, which is higher than that of many traditional photothermal agents, including

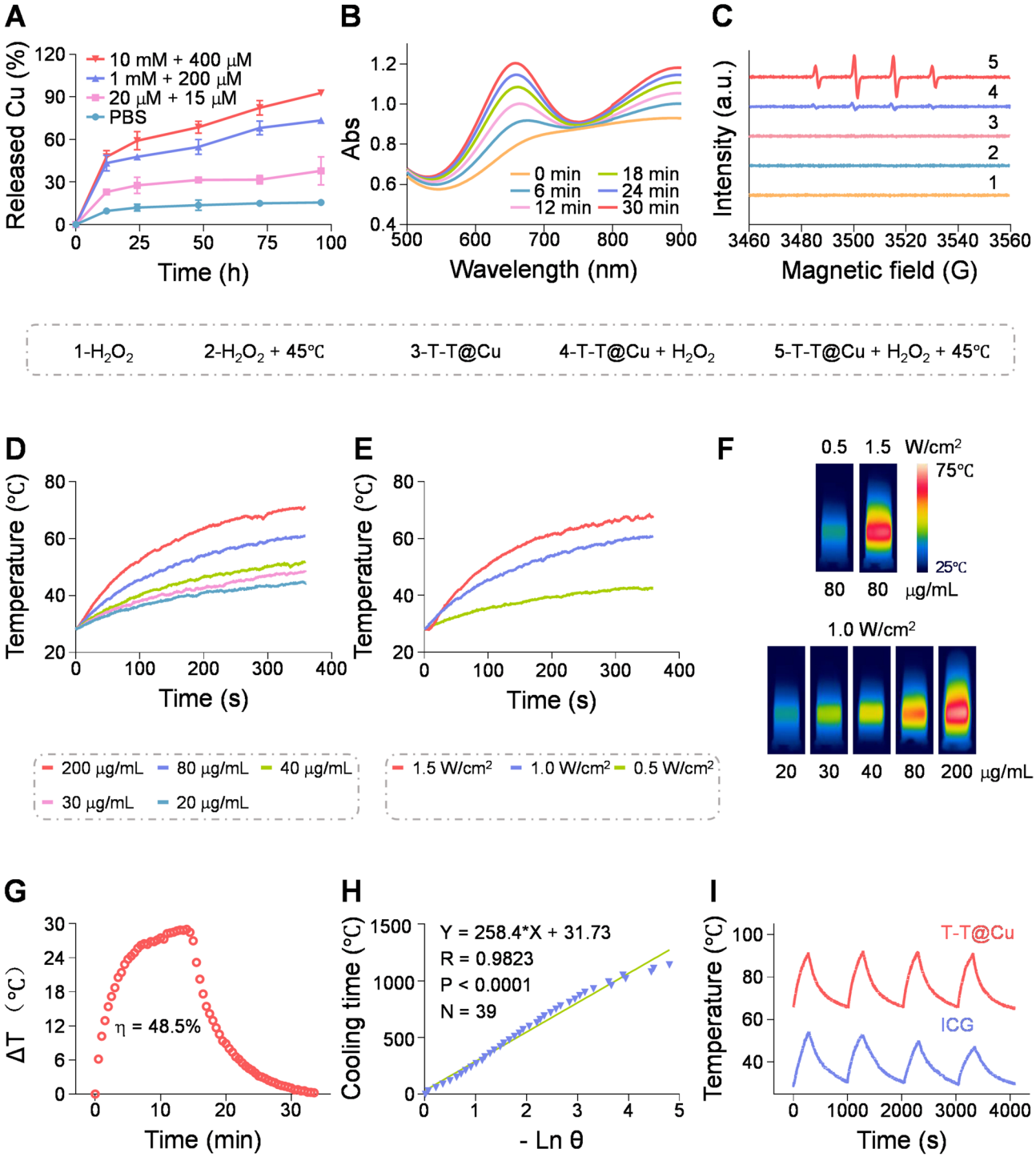

Fig. 3 In vitro •OH generation and photothermal performance study. **A**) Releasing profiles of copper ions from T-T@Cu under various mimic *in vivo* microenvironments. **B**) UV-vis absorption spectra of TMB incubated with T-T@Cu and H_2O_2 under a 1064 nm laser irradiation for different time intervals. **C**) ESR spectra of various treatment groups for the detection of •OH generation. **D**) Heating curves of T-T@Cu at different mass concentrations under a 1064 nm (1 w/cm^2) laser for 6 min. **E**) Heating curves of T-T@Cu (80 μg/mL) under a 1064 nm laser with different power density for 6 min. **F**) Infrared thermal images of T-T@Cu at different mass concentrations after irradiated by a 1064 nm laser with different power density for 6 min. **G**) Temperature variation curve of T-T@Cu during a 1064 nm laser ON/OFF cycle. **H**) Plot of linear fitting curve of cooling time versus − ln (q) of T-T@Cu. **I**) Photothermal stability of T-T@Cu and ICG over four cycles of a 1064 nm laser ON/OFF irradiation

polydopamine NPs (~ 40%), polypyrrole NPs (~ 45%), and Au NPs (~ 22%) [43, 44].The photostability analysis indicated that there was no impairment of the photothermal performance of T-T@Cu after four ON/OFF cycles of laser irradiation. In contrast, the photothermal performance of indocyanine green (ICG), a food and drug administration (FDA) approved photothermal agent, was found to gradually deteriorate under the same irradiation conditions (Fig. 3I). These results demonstrate the outstanding NIR II photothermal performance of T-T@Cu, suggesting its potential as a promising photothermal nano-agent for cancer therapy.

Efficient cellular internalization of T-T@Cu for scavenging intracellular Cys and GSH

Cys and GSH are well-known thiol-containing metal ion chelators and intracellular antioxidants that are often overexpressed in tumor microenvironments [42, 45]. Their elevated levels facilitate the strong elimination of copper ions and reactive oxygen species (ROS), which can dramatically suppress the processes of cuprotosis and ferroptosis [46]. Therefore, scavenging intracellular Cys and GSH is considered a promising strategy to enhance cellular cuprotosis and ferroptosis for cancer therapy. Moreover, Cys is a necessary amino acid for the biosynthesis of GSH and has been reported to undergo selective reactions with the cyanide groups of TCNQ [47]. In this context, we expected that the designed T-T@Cu could effectively deplete intracellular Cys and GSH simultaneously.

Prior to evaluating the Cys and GSH scavenging activity of T-T@Cu, the cellular internalization of T-T@Cu was confirmed using flow cytometry. The results showed that the detected fluorescence signals of RhB@T-T@Cu in 4T1 cells gradually increased over a 4 h incubation period, indicating successful cellular internalization of RhB@T-T@Cu. This uptake process was found to be time-dependent (Fig. S11). Following the incubation with T-T@Cu and $CuCl_2$ for 8 h, the intracellular Cys and GSH content was measured using the Cys Colorimetric Assay Kit (Elabscience) and the Reduced Glutathione (GSH) Content Assay Kit (Solarbio), respectively. As shown in Fig. S12A&12B, intracellular Cys and GSH content decreased drastically with increasing concentrations of T-T@Cu. Although the GSH content in the $CuCl_2$ treated group showed a slight reduction, the magnitude of this reduction was significantly lower (~ 2.3-folds) compared to that observed in the T-T@Cu treated cells (Fig. S12B). These results revealed the bioactivity of T-T@Cu in Cys and GSH depletion, which is conductive for amplifying cuproptosis and ferroptosis.

Evaluation of mitochondria targeting of T-T@Cu

Considering that mitochondria are the primary targets of ferroptosis and cuproptosis, the mitochondrial targeting of T-T@Cu was analyzed using CLSM and ICP-MS. The mitochondrial colocalization CLSM images showed that the red fluorescence of RhB@T-T@Cu was highly overlapped with the green fluorescence of MitoTracker Green-labeled mitochondria, confirming the excellent mitochondrial targeting capability of T-T@Cu (Fig. 4A and B). Furthermore, mitochondria from 4T1 cells treated with PBS, $CuCl_2$, T-T@Cu and T-T@Cu + L were extracted using a cell mitochondria isolation kit (Beyotime) to determine the copper ion content *via* ICP-MS. The results indicated that the copper ion concentration in the mitochondria of T-T@Cu-treated cells was approximately 4.6-fold and 22-fold higher than that in the $CuCl_2$ and PBS-treated cells, respectively. Notably, after receiving an extra 1064 nm laser irradiation, the copper ion concentration in mitochondria of T-T@Cu treated cells further increased about 0.2-folds (Fig. 4C). The significant enrichment of copper ions in the mitochondria of T-T@Cu-treated cells suggests a potential for inducing serious cytotoxicity in 4T1 cells.

Study the cytotoxicity of T-T@Cu

Encouraged by the mitochondrial-targeted delivery of copper ions and the superior NIR II photothermal performance of T-T@Cu, the cytotoxicity of T-T@Cu toward various cell lines, including normal cells (HUVEC) and cancer cells (4T1 and HepG2), was investigated. In comparation to normal cells (HUVEC), T-T@Cu exhibited cancer cells (4T1 and HepG2) specific killing efficacy. Briefly, after 24 h of incubation, the IC_{50} value of T-T@Cu against 4T1 cells and HepG2 cells were detected to be ~ 12.87 μg/mL and ~ 11.27 μg/mL, while negligible cytotoxicity was detected in HUVEC cells incubated with T-T@Cu at the same concentration (Fig. 4D). As a control group, the IC_{50} of $CuCl_2$ toward 4T1 cells was determined to be about 7.1-folds higher than that of T-T@Cu (Fig. S13). This distinct difference in cytotoxicity can be attributed to the efficient delivery of copper ions to the mitochondria by T-T@Cu (Fig. 4C). Thereafter, the cytotoxicity of T-T@Cu under a 1064 nm laser irradiation was further evaluated. After 8 h of incubation, the cell viability of 4T1 cells in various treatment groups exhibited a concentration-dependent decline of T-T@Cu. The optimal therapeutic efficacy was observed in T-T@Cu + L treatment group. Noteworthy, when a cuprotosis inhibitor (ammonium tetrathiomolybdate (ttm)) or a ferroptosis inhibitor (ferrostatin-1 (Fer-1)) were added, the cell viability of 4T1 cells in the corresponding treatment groups increased slightly. This observation provides evidence for the occurrence of cuprotosis and ferroptosis in 4T1 cells (Fig. 4E&S14). To further evaluate the in vitro

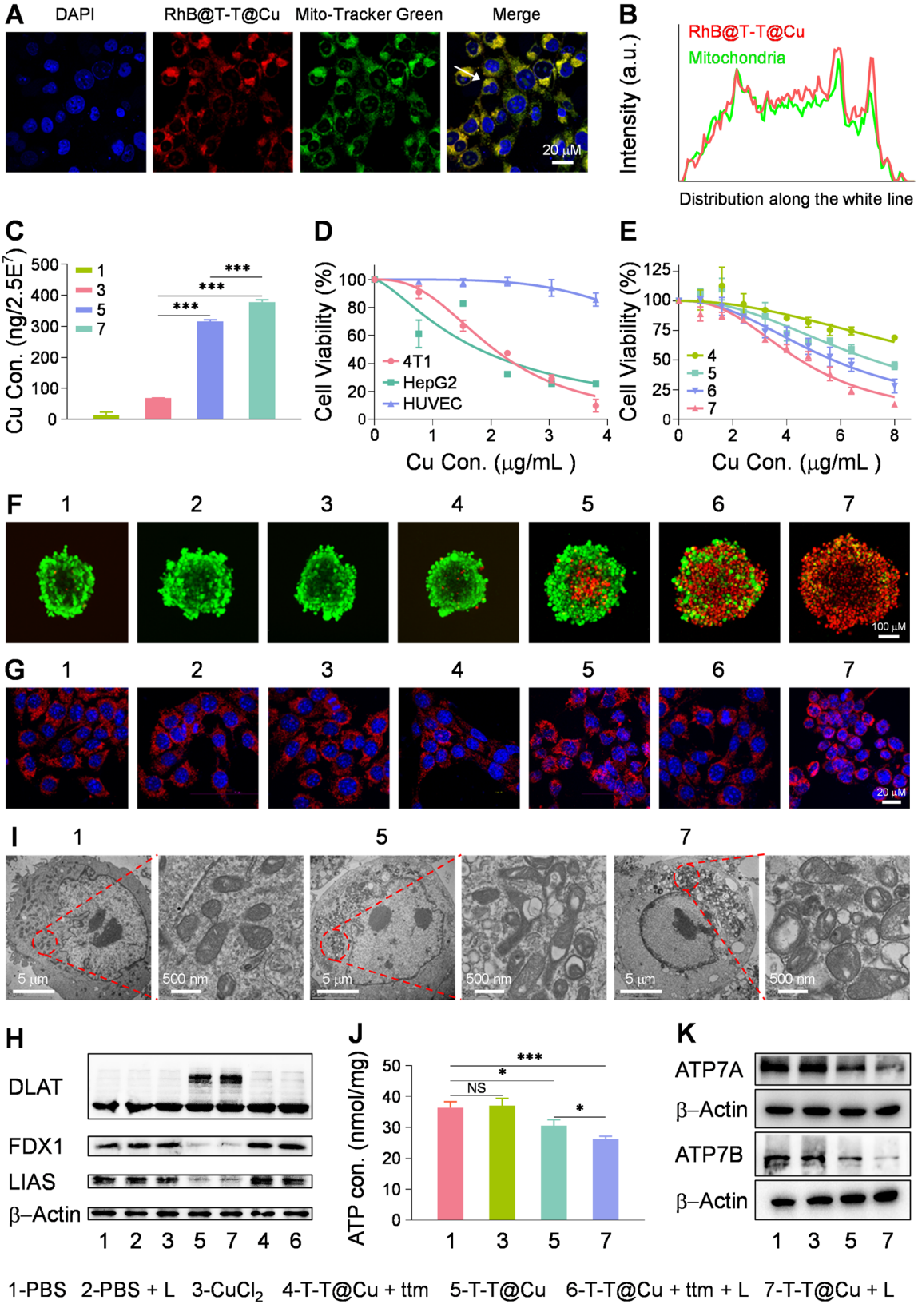

Fig. 4 (See legend on next page.)

(See figure on previous page.)

Fig. 4 T-T@Cu enable high mitochondrial enrichment and photothermal promoted cell cuproptosis and ferroptosis in 4T1 cells. **A**) Intracellular location of RhB@T-T@Cu (Red) in Mito-tracker Green labeled 4T1 cells. Nuclei were labeled with DAPI (blue). The bar value is 20 μm. **B**) Mitochondria colocalization analysis of T-T@Cu in 4T1 cells. **C**) Quantification of copper ions concentration (Con.) of isolated mitochondria from various treatment group after 8 h of incubation by ICP-MS. **D**) Relative cell viability of tumor cells (4T1 and HePG2) and normal cells (HUVEC) after incubation with T-T@Cu for 24 h. **E**) Relative cell viability of 4T1 cells in various treatment groups after 8 h of incubation. **F**) CLSM images of 4T1 MCTs upon different treatments and dead (red) and live (green) cell staining by Calcein-AM/PI. The bar value is 100 μm. **G**) Immunofluorescence images of DLAT protein in 4T1 cells of various treatment groups. The bar value is 20 μm. **H**) WB analysis on the expression levels of DLAT, FDX1 and LIAS proteins in 4T1 cells of various treatment groups. **I**) Representative TEM images of 4T1 cells after different treatments. The red dash line highlighted the cellular mitochondria. **J**) Intracellular ATP levels of 4T1 cells after different treatments. **K**) WB analysis on the expression levels of copper-ion-efflux proteins ATP7A and ATP7B in various treatment groups. Data are denoted as mean ± SD. *p*-values were calculated using Student's t-test. *$p < 0.05$, **$p < 0.01$, ***$p < 0.001$, NS represents no significance

antitumor efficacy, multicellular tumor spheroids (MCTs) of 4T1 cells receiving different treatments were stained with Calcein-AM/PI to observe live/dead cells *via* CLSM. The red fluorescence from PI-stained dead cells was found to gradually increase in the T-T@Cu, T-T@Cu + ttm + L, and T-T@Cu + L treatment groups, further confirming the satisfactory in vitro antitumor efficacy of T-T@Cu (Fig. 4F).

Exacerbate tumor cells cuproptosis via mild-photothermal boosted ferroptosis

To elucidate whether the mechanisms of cell death were indeed ferroptosis and cuproptosis, we further investigated the hallmarks of ferroptosis including intracellular ROS, LPO levels and ferroptosis-related protein, as well as the expression levels of cuproptosis-related protein across various treatment groups. Firstly, we employed 2′,7′-dichlorodihydrofluorescein diacetate (DCFH-DA) as a ROS probe to quantitatively analyze intracellular ROS levels *via* flow cytometry. As shown in Fig. S15A&S15B, the fluorescence intensity of DCFH-DA-labeled intracellular ROS in the T-T@Cu and T-T@Cu + L treatment groups was found to be 4.4-folds and 6.0-folds higher, respectively, compared to the cells treated with PBS. This indicates the superior ROS production capacity of T-T@Cu in 4T1 cells [48]. Notably, after an additional irradiation with a 1064 nm laser, the fluorescence intensity of DCFH-DA-labeled intracellular ROS in the T-T@Cu treatment group was dramatically enhanced, indicating the promotion of mild-photothermal effects on ROS generation. Subsequently, BODIPY™ 581/591 C11 were used to quantitatively analyze intracellular LPO level, another hallmark of ferroptosis, *via* flow cytometry. BODIPY™ 581/591 C11 acts as a LPO sensor that transitions its fluorescence from red to green upon oxidation by LPO. As a results, T-T@Cu + L treatment group showed the highest ratios of green fluorescence to red fluorescence, indicating robust intracellular LPO accumulation for triggering mild-photothermal boosted cell ferroptosis (Fig. S16A-S16D). Furthermore, Western blot (WB) analysis confirmed that T-T@Cu treatment significantly downregulated GPX4, a key ferroptosis marker protein, in 4T1 cells (Fig. S17). Notably, this suppression was further enhanced upon laser irradiation, suggesting that the mild photothermal effect of T-T@Cu synergistically amplifies ferroptosis signaling. Subsequently, we analyzed the hallmarks of cuproptosis, specifically focusing on lipoylated dihydrolipoamide acetyltransferase (DLAT), ferredoxin (FDX1), and lipoyl synthase (LIAS) proteins using immunofluorescence and WB analysis. The immunofluorescence images of 4T1 cells treated with PBS, PBS + L, $CuCl_2$, T-T@Cu + ttm and T-T@Cu + ttm + L showed a uniformly distributed DLAT protein with no obvious foci detected. In contrast, 4T1 cells treated with T-T@Cu and T-T@Cu + L exhibited pronounced DLAT foci, indicating that T-T@Cu can induce the formation of DLAT protein oligomers in these cells (Fig. 4G). Besides, the WB results demonstrated a significant upregulation of DLAT protein oligomers in the T-T@Cu and T-T@Cu + L treatment groups. Conversely, the expression levels of FDX1 and LIAS proteins in these groups were dramatically downregulated. In particular, after irradiation with a 1064 nm laser, the variation amplitude of the expression levels of DLAT protein oligomers, FDX1 and LIAS in T-T@Cu treatment group were further increased, which might be ascribe to the exacerbation of cell cuproptosis by the mild-photothermal boosted ferroptosis. Notably, when the cuproptosis inhibitor ttm was added to the T-T@Cu and T-T@Cu + L treatment groups, the expression levels of DLAT protein oligomers, FDX1, and LIAS proteins returned to levels similar to those observed in the PBS treatment group (Fig. 4H). Moreover, the level of DLAT protein oligomers in 4T1 cells was found to be further upregulated with increasing concentrations of T-T@Cu, while the expression levels of FDX1 and LIAS proteins were detected to be downregulated (Fig. S18). These results collectively demonstrated that T-T@Cu + L treatment can indeed induce the proteotoxic aggregation of lipoylated DLAT, as well as the destabilization of FDX1 and LIAS proteins, indicating the occurrence of photothermal-enhanced cell cuproptosis.

To gain deeper insight into the influence of mild-photothermal-boosted ferroptosis on the process of cell cuproptosis, 4T1 cells were incubated with $CuCl_2$ and T-T@Cu at the same copper ion concentration for various time intervals, followed by different treatments ($CuCl_2$, T-T@Cu and T-T@Cu + L). After the incubation, the

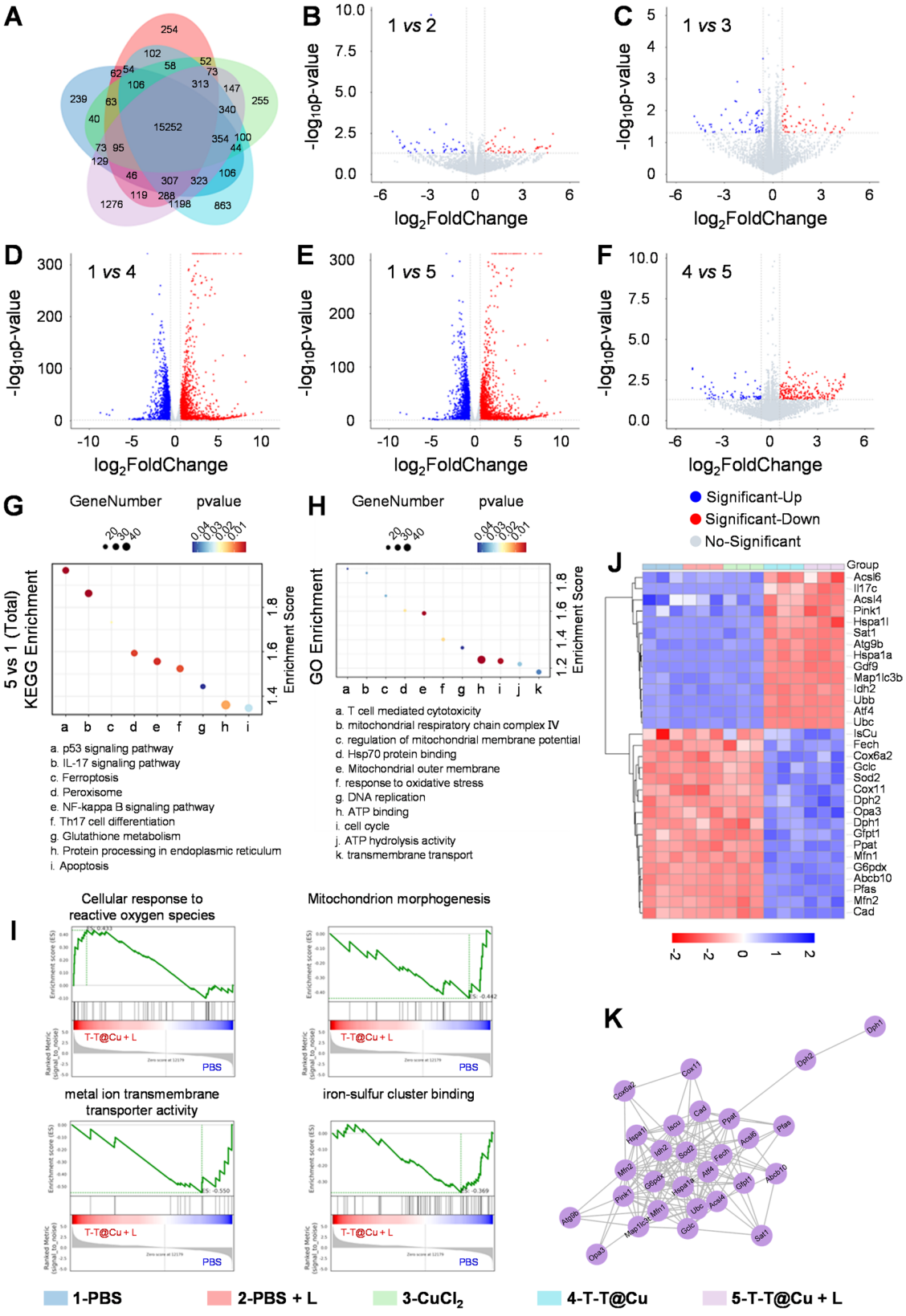

Fig. 5 (See legend on next page.)

(See figure on previous page.)

Fig. 5 Transcriptomic analysis upon RNA-sequencing reveals the anti-cancer mechanism. **A**) A Venn diagram revealed the intersection of the gene expression level of each treatment group. **B-F**) Volcano plots of different treatment groups showed the differentially expressed genes. **G**) KEGG and **H**) GO pathway enrichment analysis between PBS and T-T@Cu + L treatment groups. **I**) GSEA showed the gene sets of Cellular response to reactive oxygen species, Mitochondrion morphogenesis, metal ion transmembrane transporter activity and iron-sulfur cluster binding pathways. **J**) Heat map of differentially transcribed genes of interest of 4T1 cells in various treatment groups. **K**) Protein–protein interaction network (PPI)

intracellular copper ion concentration in 4T1 cells was quantified by ICP-MS. As depicted in Fig. S19, the highest intracellular copper ion concentration was detected in the T-T@Cu + L treatment group, regardless of whether the incubation time was 6, 8, or 10 h. Notably, after 8 h of incubation, the intracellular copper ion concentration in the T-T@Cu + L treatment group was found to be 5.4-fold higher than that in the $CuCl_2$ treatment group and 1.5-fold higher than that in the T-T@Cu treatment group. These results suggested that mild-photothermal treatment enhanced the enrichment of intracellular copper ions, thereby leading to increased cell cuproptosis. Numerous studies have shown that excessive intracellular ROS can cause significant mitochondrial damage, leading to reduced levels of adenosine triphosphate (ATP), which is crucial for the expression of copper-ion-efflux proteins ATP7A and ATP7B [49, 50]. Given our previous findings that photothermal treatment can elevate intracellular ROS levels, we speculated that the high levels of intracellular copper ion enrichment might be attributed to the mild-photothermal-induced downregulation of ATP7A and ATP7B, resulting in decreased copper ion efflux. To validate this hypothesis, we observed mitochondrial morphology using TEM and quantitatively analyzed intracellular ATP and ATP7A/7B protein levels across various treatment groups. As shown in Fig. 4I&S20, ROS induced mitochondrial damage was observed, including decreased mitochondrial volume, reduced or absent cristae, and increased membrane density in the T-T@Cu and T-T@Cu + L treatment groups. Subsequently, to assess mitochondrial membrane potential (ΔΨm), JC-1 staining was performed followed by confocal laser scanning microscopy (CLSM) analysis. Compared to PBS-treated controls, cells treated with T-T@Cu or T-T@Cu + L showed progressive ΔΨm loss, evidenced by reduced JC-1 aggregation (red fluorescence) in mitochondria. This manifested as a marked increase in green fluorescence (JC-1 monomers) concomitant with a decrease in red fluorescence (JC-1 aggregates) (Figure S21). These results confirm that both T-T@Cu and T-T@Cu + L induce mitochondrial depolarization, ultimately causing severe mitochondrial impairment. Furthermore, the intracellular ATP levels in the T-T@Cu and T-T@Cu + L treatment groups were determined to be 0.16-folds and 0.28-folds lower than that in the PBS treatment group, confirming significant down-regulation of ATP levels due to these treatments (Fig. 4J). In addition, the expression of ATP7A and ATP7B proteins in T-T@Cu and T-T@Cu + L treatment groups were found to be dramatically inhibited. Particularly, after irradiation, the expression levels of ATP7A and ATP7B proteins in the T-T@Cu treatment group were further down-regulated (Fig. 4K). These results demonstrated that mild-photothermal treatment leaded to the down-regulation of copper-ion-efflux proteins ATP7A and ATP7B, which helped maintain high intracellular copper ion concentrations and further exacerbated cell cuproptosis.

Transcriptomic analysis of anti-cancer mechanism via RNA sequencing

RNA sequencing is a powerful technology that enables high-throughput sequencing of the transcriptome, identification of differentially expressed genes, and facilitates enrichment analysis using the Kyoto Encyclopedia of Genes and Genomes (KEGG), Gene Ontology (GO), Reactome, and WikiPathways. Herein, transcriptomic analysis was conducted *via* RNA sequencing to elucidate the anti-cancer mechanisms underlying the treatment of 4T1 cells across various experimental groups. Among the genes analyzed, 3262 and 3754 genes were uniquely expressed in 4T1 cells treated with T-T@Cu and T-T@Cu + L, respectively, indicating a significant impact of these treatments on cellular gene expression (Fig. 5A). Comparative analysis with the PBS treatment group revealed that 50, 61, 2872, and 3132 genes were significantly up-regulated, while 48, 69, 2004, and 2082 genes were significantly down-regulated in the PBS + L, $CuCl_2$, T-T@Cu, and T-T@Cu + L treatment groups, respectively (Fig. 5B-E). Furthermore, in comparison to T-T@Cu treatment group, 4T1 cells in T-T@Cu + L treatment group showed 242 down-regulated genes and 77 up-regulated genes (Fig. 5F). KEGG and GO enrichment analyses of the differentially expressed genes indicated that multiple signaling pathways were significantly affected following T-T@Cu + L treatment. Notably, the glutathione metabolism pathway was significantly impacted, suggesting that T-T@Cu depletes GSH, thereby enhancing cellular cuproptosis and ferroptosis. Additionally, the enrichment of the ferroptosis pathway indicated its activation in 4T1 cells post-treatment with T-T@Cu + L, while interference with the mitochondrial respiratory chain complex IV pathway and ATP binding pathway might have contributed to alterations in intracellular ATP levels [51, 52]. Moreover, T-T@Cu + L treatment greatly influenced genes related to p53 signaling pathway and cell cycle pathway, both of which are associated with cuproptosis

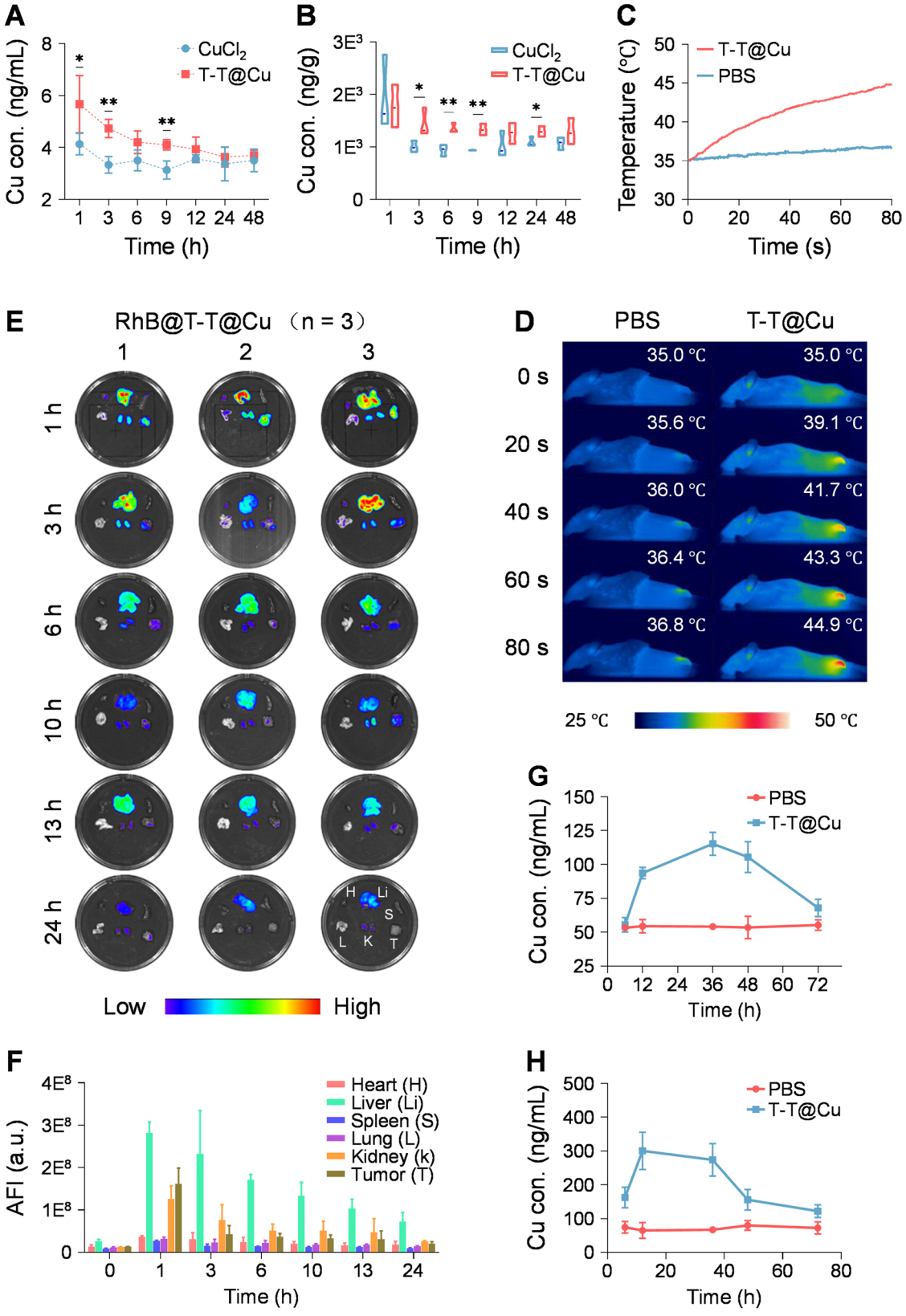

Fig. 6 (See legend on next page.)

(See figure on previous page.)

Fig. 6 *In vivo* biodistribution and metabolism of T-T@Cu. **A**) Pharmacokinetic analysis of $CuCl_2$ and T-T@Cu *via* ICP-MS quantification of copper ion concentration in blood. **B**) Copper ion concentrations of dissected tumors from $CuCl_2$ and T-T@Cu treated mice at predesigned time intervals. **C**) Temperature variation curves of tumors of mice received intravenous injection of PBS and T-T@Cu during 80 s of irradiation. **D**) Time-resolved infrared photothermal images of 4T1 tumor-bearing mice in different treatment groups. **E**) Ex vivo fluorescence distribution images of dissected main organs and tumors from RhB@T-T@Cu treatment groups ($n = 3$) at predesigned time intervals after intravenous administration. **F**) Average fluorescence intensity semiquantitative analysis of excised main organs and tumors of mice in various treatment groups. Time-dependent excretion of copper ions from **G**) feces and **H**) urine of mice received intravenous administration of PBS and T-T@Cu. Data are denoted as mean ± SD. *p*-values were calculated using Student's t-test. $^{*}p < 0.05$, $^{**}p < 0.01$, $^{***}p < 0.001$

[53, 54]. Notably, several immune-related pathways, including NF-kappa B signaling pathway, Th17 cell differentiation pathway, and T cell-mediated cytotoxicity pathway, were significantly enriched in 4T1 cells, suggesting that T-T@Cu + L treatment may potentially elicit an immune response *in vivo* (Fig. 5G and H).

To further investigate the anti-cancer mechanisms, Gene Set Enrichment Analysis (GSEA) was performed to explore specific changes in relevant pathways. The results indicated an enhancement of the cellular response to reactive oxygen species pathway, alongside the inhibition of pathways related to mitochondrion morphogenesis, metal ion transmembrane transporter activity, and iron-sulfur cluster binding, which aligns with the KEGG results and further supports that T-T@Cu + L exacerbates cuproptosis in tumor cells through mild photothermal-boosted ferroptosis (Fig. 5I). Additionally, the heat map generated from the various treatment groups revealed the major differentially expressed genes (Fig. 5J). Notably, genes associated with the iron-sulfur cluster binding pathway (e.g., Iscu, Fech, Dph1, and Dph2) and the ferroptosis pathway (e.g., Acsl4, Acsl6, Map1lc3b, and Sat1) exhibited significant down-regulation or up-regulation in the T-T@Cu and T-T@Cu + L treatment groups, indicating successful induction of cellular cuproptosis and ferroptosis. Furthermore, genes involved in ATP synthesis, including Cox11, Cox6a2, Mfn2, and Mfn1, were down-regulated in the T-T@Cu and T-T@Cu + L treatment groups, suggesting that high levels of intracellular oxidative stress inhibit ATP synthesis, consistent with previous quantitative assessments of intracellular ATP levels. Finally, a protein-protein interaction (PPI) network was plotted to illustrate the relationships among the corresponding proteins in the relevant pathways (Fig. 5K).

In vivo biosafety evaluation of T-T@Cu

Prior to *in vivo* application, the biosafety of T-T@Cu was thoroughly evaluated through several assays, including hemolysis assessment, blood biochemical analysis, and histological examination *via* H&E staining. The hemolysis ratio of T-T@Cu at a mass concentration of up to 80 μg/mL was determined to be 3.3%. This low hemolysis ratio indicated excellent hemocompatibility of T-T@Cu, as well as its feasibility for intravenous administration (Fig. S22). Blood biochemical analysis was conducted on day fourteen following three intravenous doses of T-T@Cu (4.4 μg/g body weight) in mice. Compared to PBS-treated mice, there were no significant differences in blood biochemical indices, including ALT, AST, BUN, CREA, CK, and CK-MB, in mice treated with T-T@Cu. This suggested that there was no loss of cardiac and hepatorenal function in the treated mice (Fig. S23A). Besides, H&E staining was performed on the main organs, including the heart, liver, spleen, lung, and kidney, from T-T@Cu-treated mice. The H&E staining images revealed no serious cell damage, such as changes in cell morphology or condensed nuclei, further demonstrating the biosafety of T-T@Cu for potential *in vivo* applications (Fig. S23B).

In vivo biodistribution and metabolism of T-T@Cu

To address complex clinical demands, ideal nanodrugs should exhibit multiple functionalities, including prolonged blood circulation, specific tumor-targeting, and effective metabolism [55]. Therefore, we systematically investigated the *in vivo* biodistribution and metabolism of T-T@Cu following intravenous administration in mice using ex vivo fluorescence imaging and ICP-MS analysis. Compared to $CuCl_2$ treated mice, the half-life of copper in the blood of T-T@Cu treated mice was found significantly prolonged, which guaranteed the subsequent ongoing accumulation of T-T@Cu in tumors (Fig. 6A). ICP-MS analysis revealed that the intra-tumoral copper content in T-T@Cu-treated mice was much higher than that in $CuCl_2$ treated mice, confirming the specific tumor-targeting capability of T-T@Cu (Fig. 6B). Furthermore, *in vivo* infrared photothermal imaging was conducted on PBS and T-T@Cu-treated mice. As shown in Fig. 6C and D, negligible temperature increase was observed in PBS-treated mice, while T-T@Cu-treated mice exhibited significant temperature variation, with tumor site temperatures reaching approximately 45℃ after 80 s of irradiation. This temperature rise further supported the substantial accumulation of T-T@Cu at the tumor site. Additionally, fluorescence images of dissected tissues, including heart, liver, spleen, lung, kidney, intestine and tumor, were obtained at pre-designed time intervals. The fluorescence of RhB@T-T@Cu was primarily detected in the liver, kidney, intestine, and tumor of treated mice, with fluorescence intensity gradually decreasing over 24 h (Fig. 6E and F&S24). The gradual attenuation of fluorescence in these tissues might be attributed to the high expression of GSH and Cys, which induced the

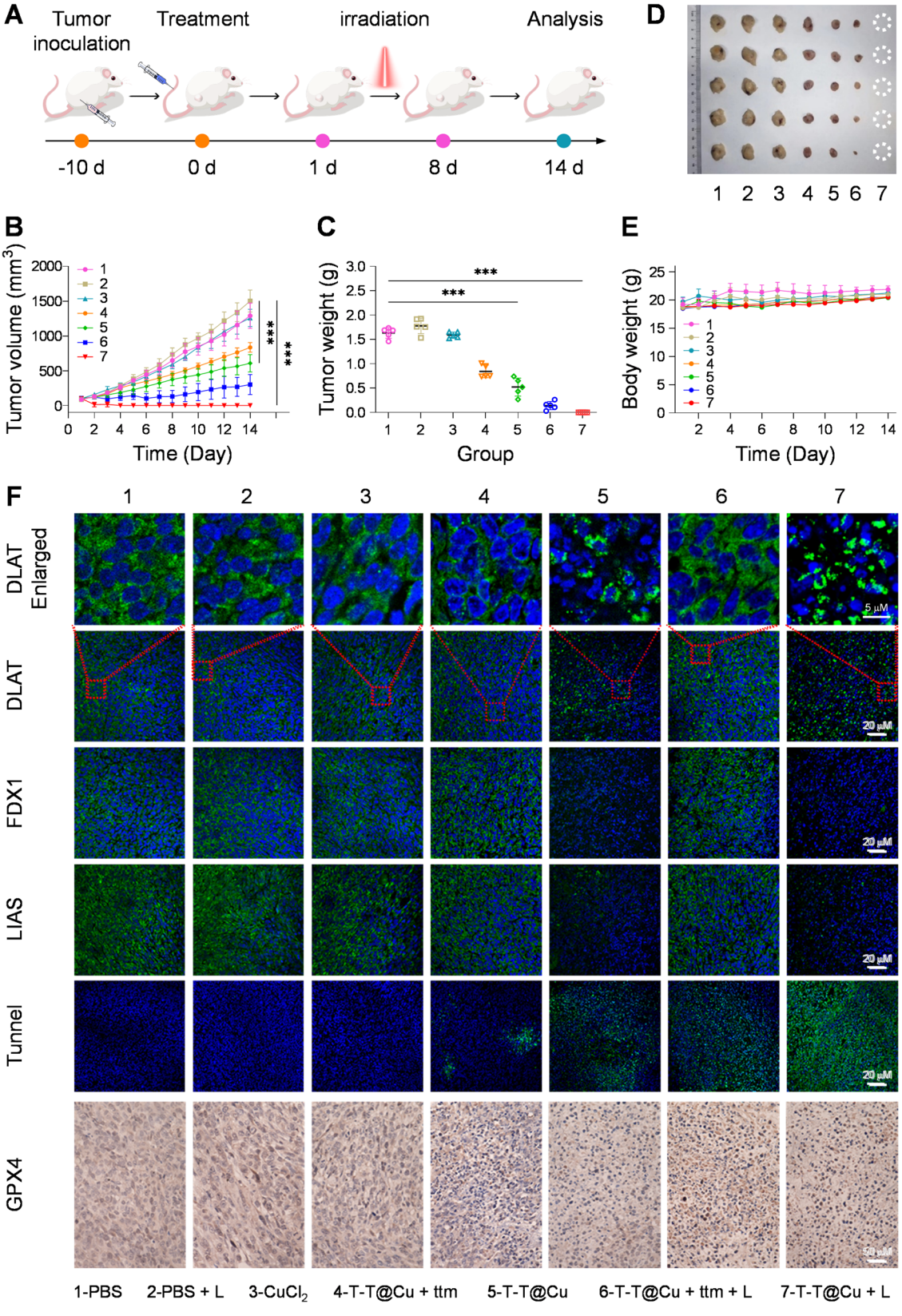

Fig. 7 (See legend on next page.)

(See figure on previous page.)

Fig. 7 Mild-photothermal promoted cell cuproptosis and ferroptosis in subcutaneous 4T1 breast tumor models. **A**) Schematic illustration of the establishment of subcutaneous 4T1 breast tumor models in mice and the therapeutic regimen. **B**) Tumor growth curves of mice upon various treatments. **C**) Ex vivo tumor weight and **D**) tumorous digital photos of mice upon various treatments. **E**) Body weight variation of mice in different treatment groups during 14 days. **F**) DLAT, FDX1, LIAS and GPX4 immunohistochemical staining as well as Tunnel staining of tumor tissue sections of each treatment groups. The green fluorescence represents DLAT, FDX1, LIAS proteins and apoptotic DNA fragmentation staining, while the blue fluorescence indicates nuclear staining. Data are denoted as mean ± SD. *p*-values were calculated using Student's t-test. *$p < 0.05$, **$p < 0.01$, ***$p < 0.001$

degradation of RhB@T-T@Cu in these tissues. To further evaluate the metabolism process of T-T@Cu *in vivo*, feces and urine from mice administered with PBS and T-T@Cu were collected for ICP-MS measurement. As depicted in Fig. 6G and H, significantly increased copper concentrations were detected in the feces and urine of T-T@Cu-treated mice within 72 h post-administration, suggesting the hepatic and renal metabolic pathways of T-T@Cu. Taken together, T-T@Cu demonstrated long blood circulation, specific tumor targeting, and effective metabolism *in vivo*, which addressed the multifaceted requirements of nanodrug delivery systems.

Exploration of in vivo anti-tumor efficacy and mechanism

Encouraged by the promising in vitro anti-cancer efficacy and the remarkable *in vivo* biosafety and tumor-targeting properties of T-T@Cu, the *in vivo* anti-tumor effect of various treatments including PBS, PBS + L, $CuCl_2$, T-T@Cu, T-T@Cu + ttm, T-T@Cu + ttm + L and T-T@Cu + L was comprehensively investigated. BABL/C mice were selected to establish a subcutaneous 4T1 tumor model. As illustrated in Fig. 7A, mice received four intravenous doses of the different drug formulations, along with three sessions of irradiation during the therapeutic period. For *in vivo* therapeutic efficacy evaluation, tumor volume, tumor weight, and body weight of the mice were monitored daily throughout the treatment. The tumor growth inhibition data revealed a dramatic suppression of tumor volume and weight in the T-T@Cu, T-T@Cu + ttm, T-T@Cu + ttm + L, and T-T@Cu + L treatment groups (Fig. 7B and C). Moreover, excised tumors demonstrated that tumors in the T-T@Cu + L treatment group were thoroughly cured (Fig. 7D). Also, H&E staining of tumor tissues from various treatment groups showed significant cellular damage, including changes in cell morphology and nuclear condensation, particularly in the T-T@Cu + L treatment group (Fig. S25). Noteworthy, the introduction of ttm significantly impaired the therapeutic efficacy of the corresponding treatment group, suggesting that cuproptosis played an important role in the tumor inhibition mechanism of T-T@Cu. Finally, no significant fluctuations in body weight were observed in the treatment groups, indicating excellent biosafety of the formulations (Fig. 7E).

To figure out the potential *in vivo* anti-tumor mechanism of T-T@Cu, the expression of cuproptosis and ferroptosis related proteins including DLAT, FDX1, LIAS and GPX4 in tumors were evaluated *via* immunofluorescence and immunohistochemical analyses. Compared to the PBS, PBS + L, $CuCl_2$, T-T@Cu + ttm, and T-T@Cu + ttm + L treatment groups, tumors treated with T-T@Cu and T-T@Cu + L exhibited a progressive increase in DLAT foci, alongside a marked reduction in FDX1, LIAS, and GPX4 expression (Fig. 7F). Notably, the significantly downregulation of GPX4 in tumor tissues, indicating ferroptosis induction *in vivo.* To further validate this, we assessed additional ferroptosis biomarkers, including intratumoral ROS levels and malondialdehyde (MDA), a downstream product of lipid peroxidation. As shown in Figure S26&S27, T-T@Cu and T-T@Cu + L treated groups showed distinct DCFH-DA marked green fluorescence of ROS and up-regulation of MDA in tumors, indicating T-T@Cu and T-T@Cu + L treatments effectively induced accumulation of intratumoral ROS and lipid peroxides. These findings provide evidence for photothermal-promoted cuproptosis and ferroptosis in these tumors. Furthermore, the administration of ttm resulted in the loss of expression variation for DLAT, FDX1, and LIAS in the T-T@Cu and T-T@Cu + L treatment groups, further supporting the involvement of cuproptosis in tumor cell death. Additionally, terminal deoxynucleotidyl transferase-mediated dUTP nick-end labeling (TUNEL) staining of tumor tissues revealed that T-T@Cu + L induced the most significant apoptosis among the treatment groups (Fig. 7F). Taken together, T-T@Cu could effectively suppresses tumor growth through the activation of cuproptosis, ferroptosis, and apoptosis pathways.

Conclusion

In summary, we successfully constructed a carrier-free metal-polyphenol nanoplatform (T-T@Cu) through the self-assembly of TA, TCNQ, and copper ions to facilitate cuproptosis in tumor cells. This nanoplatform exhibited excellent tumor-mitochondria cascade targeting, GSH depletion, Fenton-like catalytic activity, and NIR II photothermal conversion properties (h = 48.5%). Once internalized by tumor cells, T-T@Cu not only accumulated specifically in the mitochondria but also consumed the overexpressed GSH present in tumor microenvironments, alleviating GSH-induced copper inactivation. Furthermore, T-T@Cu demonstrated Cys/GSH dual-responsive degradation and controllable copper ion release features in the tumor Cys/GSH microenvironment. Upon irradiation by a 1064 nm laser, T-T@

Cu triggered mild photothermal-boosted ferroptosis in tumor cells, impacting cellular ATP synthesis. This process further disrupted intracellular copper homeostasis by downregulating the expression of copper-ion efflux proteins ATP7A/7B, leading to enhanced mitochondrial copper accumulation and exacerbated cuproptosis in tumor cells. Based on these ideal characteristics, effective tumor targeting, high tumor inhibition rate (~100%) and no obvious systematic toxicity were achieved. This novel strategy for exacerbating tumor cell cuproptosis shows great promise for future clinical applications in oncotherapy.

Supplementary Information

The online version contains supplementary material available at https://doi.org/10.1186/s12951-025-03722-2.

Supplementary Material 1.

Acknowledgements
Not applicable.

Author contributions
X.L. and S.F. contributed equally to this work. All authors have approved the final version of the manuscript.

Funding
This work was supported by the National Natural Science Foundation of China (32101138, 22277018), the Zhejiang Key Laboratory of Intelligent Cancer Biomarker Discovery and Translation (Grant No. 2018E10008), the Joint Funds of the Zhejiang Provincial Natural Science Foundation of China (Grant No. LLSSZ24H160001), the Zhejiang Provincial Natural Science Foundation for Distinguished Young Scholar (LR23B030001), the Zhejiang Science and Technology Department "vanguard" "leading goose" research (Grant No. 2023C03044), the financial support from the Wenzhou Institute, University of Chinese Academy of Sciences (WIUCASQD2022028), the financial support from the Key Laboratory for upper limb edema and breast cancer stasis diagnosis and intervention.

Data availability
No datasets were generated or analysed during the current study.

Declarations

Ethics approval and consent to participate
All animal experiments were conducted following the protocols approved by the Laboratory Animal Ethics Committee of Wenzhou Institute, University of Chinese Academy of Sciences (WIUCAS23070701). All participants consented to publish the paper.

Consent for publication
Not applicable.

Competing interests
The authors declare no competing interests.

Author details
[1]Guangxi Technology Innovation Cooperation Base of Prevention and Control Pathogenic Microbes with Drug Resistance, Youjiang Medical University for Nationalities, Baise 533000, China
[2]Wenzhou Institute, University of Chinese Academy of Sciences, Wenzhou 325001, China
[3]Zhejiang Key Laboratory of Imaging and Interventional Medicine, Zhejiang Engineering Research Center of Interventional Medicine Engineering and Biotechnology, Key Laboratory of Precision Medicine of Lishui City, the Fifth Affiliated Hospital of Wenzhou Medical University, Lishui 323000, China
[4]Postgraduate Training Base Alliance of Wenzhou Medical University (Zhejiang Provincial People's Hospital), 310000 Hangzhou, China
[5]General Surgery, Cancer Center, Department of Breast Surgery, Zhejiang Provincial People's Hospital, Affiliated People's Hospital, Hangzhou Medical College, 310014 Hangzhou, China
[6]Department of Pathology, The First Affiliated Hospital of Wenzhou Medical University, Wenzhou 325000, Zhejiang, China
[7]Zhejiang Key Laboratory of Intelligent Cancer Biomarker Discovery and Translation, First Affiliated Hospital, Wenzhou Medical University, Wenzhou 325035, China

Received: 16 April 2025 / Accepted: 16 September 2025
Published online: 10 October 2025

References

1. Tsvetkov P, Coy S, Petrova B, Dreishpoon M, Verma A, Abdusamad M, Rossen J, Joesch-Cohen L, Humeidi R, Spangler RD, Eaton JK, Frenkel E, Kocak M, Corsello SM, Lutsenko S, Kanarek N, Santagata S, Golub TR. Copper induces cell death by targeting lipoylated TCA cycle proteins. Science. 2022;375(6586):1254–61.
2. Wang W, Mo W, Hang Z, Huang Y, Yi H, Sun Z, et al. Cuproptosis: harnessing transition metal for cancer therapy. ACS Nano. 2023;17(20):19581–99.
3. Yang Y, Li M, Chen G, Liu S, Guo H, Dong X, et al. Dissecting copper biology and cancer treatment: 'Activating Cuproptosis or suppressing cuproplasia.' Coord Chem Rev. 2023;495:215395.
4. Tang D, Kroemer G, Kang R. Targeting cuproplasia and cuproptosis in cancer. Nat Rev Clin Oncol. 2024;21:370–88.
5. Qiao L, Zhu G, Jiang T, Qian Y, Sun Q, Zhao G, et al. Self-destructive copper carriers induce pyroptosis and cuproptosis for efficient tumor immunotherapy against dormant and recurrent tumors. Adv Mater. 2024;36(8):2308241.
6. Ding H, Ren F, Liu P, Feng Y, Ma X, Shen Z, et al. Cu^{2+}-anchored carbon nanophotocatalysts for visible water splitting to boost hydrogen cuproptosis. Angew Chem Int Ed. 2023;62(44):e202311549.
7. Jin XK, Liang JL, Zhang SM, Huang QX, Zhang SK, Liu CJ, Zhang XZ. Orchestrated copper-based nanoreactor for remodeling tumor microenvironment to amplify cuproptosis-mediated anti-tumor immunity in colorectal cancer. Mater Today. 2023;68:108–24.
8. Chen Y, Wang Y, Zhang R, Wang F, Lin X, Wang T, et al. In situ transformable fibrillar clusters disrupt intracellular copper metabolic homeostasis by comprehensive blockage of cuprous ions efflux. Small. 2025;21(1):2406802.
9. Guan M, Cheng K, Xie XT, Li Y, Ma MW, Zhang B, et al. Regulating copper homeostasis of tumor cells to promote Cuproptosis for enhancing breast cancer immunotherapy. Nat Commun. 2024;15:10060.
10. Zheng J, Ge H, Guo M, Zhang T, Hu Q, Yao Q, et al. Photoinduced cuproptosis with tumor-specific for metastasis-inhibited cancer therapy. Small. 2024;20(10):2304407.
11. Zu H, Wu Y, Meng H, Cheng X, Wang Y, Zhang LW, et al. Tumor metabolism aiming $Cu_{2-x}S$ nanoagents mediate photothermal-derived cuproptosis and immune activation. ACS Nano. 2024;18(35):23941–57.
12. Oliveri V. Biomedical applications of copper ionophores. Coord Chem Rev. 2020;422:213474.
13. Guo B, Yang F, Zhang L, Zhao Q, Wang W, Yin L, et al. Cuproptosis induced by ROS responsive nanoparticles with elesclomol and copper combined with aPD-L1 for enhanced cancer immunotherapy. Adv Mater. 2023;35(22):2212267.
14. Hu J, Yan L, Cao Z, Geng B, Cao X, Liu B, et al. Tumor microenvironment activated Cu crosslinked near-infrared sonosensitizers for visualized Cuproptosis-enhanced sonodynamic cancer Immunotherapy. Adv Sci. 2024;11(43):2407196.
15. Steinbrueck A, Sedgwick AC, Brewster JT, Yan KC, Shang Y, Knoll DM, Vargas-Zuniga GI, He XP, Tian H, Sessler JL. Transition metal chelators, pro-chelators, and ionophores as small molecule cancer chemotherapeutic agents. Chem Soc Rev. 2020;49(12):3726–47.
16. Wang S, Liu X, Wei D, Zhou H, Zhu J, Yu Q, Luo L, Dai X, Jiang Y, Yu L, Yang Y, Tan W. Polyvalent aptamer nanodrug conjugates enable efficient tumor

Cuproptosis therapy through copper overload and glutathione depletion. J Am Chem Soc. 2024;146(44):30033–45.
17. Wang X, Wang D, Liao Y, Guo X, Song Q, Liu W, Gu C, Du S, Sun B, Gu Z. Hafnium oxide-based sensitizer with radiation-triggered Cuproptosis for radiotherapy. Nano Today. 2025;61:102626.
18. Li Y, Liu J, Weichselbaum RR, Lin W. Mitochondria-targeted multifunctional nanoparticles combine cuproptosis and programmed cell death-1 down-regulation for cancer immunotherapy. Adv Sci. 2024;11(35):2403520.
19. Liu LH, Zhang XZ. Carrier-free nanomedicines for cancer treatment. Prog Mater Sci. 2022;125:100919.
20. Yang R, Zhan M, Shen S, Zhang B, Ouyang Z, Guo H, et al. Microfluidic synthesis of carrier-free full-active metal-phenolic nanocapsules for tumor chemo-chemodynamic-immune therapy. Adv Funct Mater. 2025;35(11):2417070.
21. Zhang N, Wang Z, Li G, Zhang M, Liu Q, Cai C, et al. A carrier-free metal-phenolic network with enhanced ferroptosis-immunotherapy for overcoming tumor resistance and metastasis. Chem Eng J. 2024;488:150780.
22. Guo Y, Sun Q, Wu FG, Dai Y, Chen X. Polyphenol-containing nanoparticles: synthesis, properties, and therapeutic delivery. Adv Mater. 2021;33(22):2007356.
23. Liu T, Ma M, Ali A, Liu Q, Bai R, Zhang K, et al. Self-assembled copper tannic acid nanoparticles: a powerful nano-bactericide by valence shift of copper. Nano Today. 2024;54:102071.
24. Zhang J, Gao B, Ye B, Sun Z, Qian Z, Yu L, et al. Mitochondrial-targeted delivery of polyphenol-mediated antioxidases complexes against pyroptosis and inflammatory diseases. Adv Mater. 2023;35(11):2208571.
25. Shin M, Lee HA, Lee M, Shin Y, Song JJ, Kang SW, et al. Targeting protein and peptide therapeutics to the heart *via* tannic acid modification. Nat Biomed Eng. 2018;2:304–17.
26. Xue Q, Kang R, Klionsky DJ, Tang D, Liu J, Chen X. Copper metabolism in cell death and autophagy. Autophagy. 2023;19(8):2175–95.
27. Zhang W, Chen Z, Xiong C, Yuan L, Hu JJ, Dai J, et al. A peptide-copper self-assembled nanoparticle for enhanced Cuproptosis by metabolic reprogramming in tumor cells. ACS Nano. 2024;18(50):34244–56.
28. Shanbhag V, Jasmer-McDonald K, Zhu S, Martin AL, Gudekar N, Khan A, et al. ATP7A delivers copper to the lysyl oxidase family of enzymes and promotes tumorigenesis and metastasis. Proc Natl Acad Sci USA. 2019;116(14):6836–41.
29. Chen W, Xie W, Gao Z, Lin C, Tan M, Zhang Y, et al. Mild-photothermal effect induced high efficiency Ferroptosis-Boosted-Cuproptosis based on Cu_2O@$Mn_3Cu_3O_8$ nanozyme. Adv Sci. 2023;10(33):2303694.
30. Zhang X, Zhu J, Wang S, Li S, Hu EJ, Mou J, Ding R, Yang H, Xie P. A Copper/Ferrous-Engineering redox homeostasis disruptor for Cuproptosis/Ferroptosis Co-Activated nanocatalytic therapy in liver cancer. Adv Funct Mater. 2024;34(37):2402022.
31. Huang L, Zhu J, Wu G, Xiong W, Feng J, Yan C, et al. A strategy of adding fuel to the flames enables a self-accelerating cycle of ferroptosis-cuproptosis for potent antitumor therapy. Biomaterials. 2024;311:122701.
32. Ning S, Lyu M, Zhu D, Lam JWY, Huang Q, Zhang T, et al. Type-I AIE photosensitizer loaded biomimetic system boosting cuproptosis to inhibit breast cancer metastasis and rechallenge. ACS Nano. 2023;17(11):10206–17.
33. Ge H, Du J, Zheng J, Xu N, Yao Q, Long S, Fan J, Peng X. Effective treatment of cisplatin-resistant ovarian tumors with a MoS_2-based sonosensitizer and nanoenzyme capable of reversing the resistant-microenvironment and enhancing ferroptosis and apoptosis. Chem Eng J. 2022;446(3):137040.
34. Liang H, Wu X, Zhao G, Feng K, Ni K, Sun X. Renal clearable ultrasmall single-crystal Fe nanoparticles for highly selective and effective ferroptosis therapy and immunotherapy. J Am Chem Soc. 2021;143(38):15812–23.
35. Hu R, Fang Y, Huo M, Yao H, Wang C, Chen Y, et al. Ultrasmall $Cu_{2-x}S$ nanodots as photothermal-enhanced fenton nanocatalysts for synergistic tumor therapy at NIR-II biowindow. Biomaterials. 2019;206:101–14.
36. Huang Y, Wang Z, Chen Z, Zhang Q. Organic cocrystals: beyond electrical conductivities and field-effect transistors (FETs). Angew Chem Int Ed. 2019;58(29):9696–711.
37. Tang B, Li WL, Chang Y, Yuan B, Wu Y, Zhang MT, et al. A supramolecular radical dimer: high-efficiency NIR-II photothermal conversion and therapy. Angew Chem Int Ed. 2019;58(43):15526–31.
38. Wei D, Sun Y, Zhu H, Fu Q. Stimuli-responsive polymer-based nanosystems for cancer theranostics. ACS Nano. 2023;17(23):23223–61.
39. Liu S, Tang A, Xie M, Zhao Y, Jiang J, Liang G. Oligomeric hydrogels self-assembled from reduction-controlled condensation. Angew Chem Int Ed. 2015;54(12):3639–42.
40. Zhao F, Yu H, Liang L, Wang C, Shi D, Zhang X, Ying Y, Cai W, Li W, Li J, Zheng J, Qiao L, Che S, Yu J. Redox homeostasis disruptors based on Metal-Phenolic network nanoparticles for Chemo/Chemodynamic synergistic tumor therapy through activating apoptosis and Cuproptosis. Adv Healthc Mater. 2023;12(29):2301346.
41. Cheng R, Feng F, Meng F, Deng C, Feijen J, Zhong Z. Glutathione-responsive nano-vehicles as a promising platform for targeted intracellular drug and gene delivery. J Control Release. 2011;152(1):2–12.
42. Su S, Li X, An Q, Liang T, Wang Y, Deng H, Xiong X, Wong W-L, Zhang H, Li C. A smart cysteine-activated and heavy-atom-free nano-photosensitizer for photodynamic therapy to treat cancers. Chem Commun. 2024;60(29):3910–3.
43. Wang Q, Wang G, Li X, Li D, Zhang C, Ding J. Photothermal effect and biomineralization of black phosphorus nanosheet-composited hydrogel boosts synergistic treatment of dentin hypersensitivity. Adv Sci. 2025;12(9):2412561.
44. Wu D, Fei F, Zhang Q, Wang X, Gong Y, Chen X, et al. Nanoengineered on-demand drug delivery system improves efficacy of pharmacotherapy for epilepsy. Sci Adv. 2022;8(2):eabm3381.
45. Su J, Gu M, Peng L, Guo J, Chen P, Wen Y, et al. A self-assembled nano-molecular glue (Nano-mGlu) enables GSH/H_2O_2-triggered targeted protein degradation in cancer therapy. J Am Chem Soc. 2025;147(1):372–83.
46. Xu W, Qian J, Hou G, Wang T, Wang J, Wang Y, et al. A hollow amorphous bimetal organic framework for synergistic Cuproptosis/Ferroptosis/Apoptosis anticancer therapy *via* disrupting intracellular redox homeostasis and Copper/Iron metabolisms. Adv Funct Mater. 2022;32(40):2205013.
47. Ou C, Na W, Ge W, Huang H, Gao F, Zhong L, et al. Biodegradable charge-transfer complexes for glutathione depletion induced ferroptosis and NIR-II photoacoustic imaging guided cancer photothermal therapy. Angew Chem Int Ed. 2021;60(15):8157–63.
48. Liu Y, Quan X, Li J, Huo J, Li X, Zhao Z, et al. Liposomes embedded with pegylated iron oxide nanoparticles enable ferroptosis and combination therapy in cancer. Natl Sci Rev. 2023;10(1):nwac167.
49. Liu Z, Liu S, Liu B, Meng Q, Yuan M, Ma X, et al. Facile synthesis of Fe-based metal-quinone networks for mutually enhanced mild photothermal therapy and ferroptosis. Angew Chem Int Ed. 2025;64(2):e202414879.
50. Du Y, Zhao X, He F, Gong H, Yang J, Wu L, et al. A vacancy-engineering ferroelectric nanomedicine for Cuproptosis/Apoptosis co-activated immunotherapy. Adv Mater. 2024;36(30):2403253.
51. Vercellino I, Sazanov LA. The assembly, regulation and function of the mitochondrial respiratory chain. Nat Rev Mol Cell Biol. 2022;23:141–61.
52. Taruno A. ATP release channels. Int J Mol Sci. 2018;19(3):808.
53. Liao Q, Deng J, Tong J, Gan Y, Hong W, Dong H, et al. p53 induces circFRMD4A to suppress cancer development through glycolytic reprogramming and cuproptosis. Mol Cell. 2025;85(1):132–49.
54. Lu S, Li Y, Yu Y. Glutathione-scavenging celastrol-Cu nanoparticles induce self-amplified cuproptosis for augmented cancer immunotherapy. Adv Mater. 2024;36(35):2404971.
55. Zhou Q, Xiang J, Qiu N, Wang Y, Piao Y, Shao S, et al. Tumor abnormality-oriented nanomedicine design. Chem Rev. 2023;123(18):10920–89.

Publisher's note